nanomaterials

MDPI

Article

Decoding the Atomic Structure of Ga_2Te_5 Pulsed Laser Deposition Films for Memory Applications Using Diffraction and First-Principles Simulations

Andrey Tverjanovich [1], Chris J. Benmore [2], Maxim Khomenko [3,4], Anton Sokolov [5], Daniele Fontanari [5], Sergei Bereznev [6], Maria Bokova [5], Mohammad Kassem [5] and Eugene Bychkov [5,*]

1 Institute of Chemistry, St. Petersburg State University, 198504 St. Petersburg, Russia; andr.tver@yahoo.com
2 X-ray Science Division, Advanced Photon Source, Argonne National Laboratory, Argonne, IL 60439, USA; benmore@anl.gov
3 ILIT RAS-Branch of the FSRC "Crystallography and Photonics" RAS, 140700 Moscow, Russia; khomenkolaser@gmail.com
4 Laboratory of Biophotonics, Tomsk State University, 634050 Tomsk, Russia
5 Laboratoire de Physico-Chimie de l'Atmosphère, Université du Littoral Côte d'Opale, 59140 Dunkerque, France; anton.sokolov@univ-littoral.fr (A.S.); danielefontanari@gmail.com (D.F.); maria.bokova@univ-littoral.fr (M.B.); mohamad.kassem@univ-littoral.fr (M.K.)
6 Department of Materials and Environmental Technology, Tallinn University of Technology, 19086 Tallinn, Estonia; sergei.bereznev@taltech.ee
* Correspondence: eugene.bychkov@univ-littoral.fr

Abstract: Neuromorphic computing, reconfigurable optical metamaterials that are operational over a wide spectral range, holographic and nonvolatile displays of extremely high resolution, integrated smart photonics, and many other applications need next-generation phase-change materials (PCMs) with better energy efficiency and wider temperature and spectral ranges to increase reliability compared to current flagship PCMs, such as $Ge_2Sb_2Te_5$ or doped Sb_2Te. Gallium tellurides are favorable compounds to achieve the necessary requirements because of their higher melting and crystallization temperatures, combined with low switching power and fast switching rate. Ga_2Te_3 and non-stoichiometric alloys appear to be atypical PCMs; they are characterized by regular tetrahedral structures and the absence of metavalent bonding. The sp^3 gallium hybridization in cubic and amorphous Ga_2Te_3 is also different from conventional p-bonding in flagship PCMs, raising questions about its phase-change mechanism. Furthermore, gallium tellurides exhibit a number of unexpected and highly unusual phenomena, such as nanotectonic compression and viscosity anomalies just above their melting points. Using high-energy X-ray diffraction, supported by first-principles simulations, we will elucidate the atomic structure of amorphous Ga_2Te_5 PLD films, compare it with the crystal structure of tetragonal gallium pentatelluride, and investigate the electrical, optical, and thermal properties of these two materials to assess their potential for memory applications, among others.

Keywords: phase-change materials; synchrotron diffraction; first-principles molecular dynamics

Citation: Tverjanovich, A.; Benmore, C.J.; Khomenko, M.; Sokolov, A.; Fontanari, D.; Bereznev, S.; Bokova, M.; Kassem, M.; Bychkov, E. Decoding the Atomic Structure of Ga_2Te_5 Pulsed Laser Deposition Films for Memory Applications Using Diffraction and First-Principles Simulations. *Nanomaterials* **2023**, *13*, 2137. https://doi.org/10.3390/nano13142137

Academic Editor: Junying Zhang

Received: 15 June 2023
Revised: 12 July 2023
Accepted: 19 July 2023
Published: 23 July 2023

1. Introduction

Brain-inspired computing [1–3], light-controlled (i.e., over a wide spectral range, from visible to THz) or electrically controlled reconfigurable optical metamaterials [4–6], high resolution holographic and nonvolatile displays [7,8], integrated photonic circuits [9,10], and many other applications need next-generation phase-change materials (PCMs) with better energy efficiency and wider temperature and spectral ranges to increase reliability compared to current flagship PCMs, such as $Ge_2Sb_2Te_5$, doped Sb_2Te, etc. Gallium tellurides seem to be promising candidates to achieve the necessary requirements because of their higher melting and crystallization temperatures, combined with low switching

power and fast switching rate [11–13]. Ga_2Te_3 and non-stoichiometric compositions appear to be atypical PCMs; they are characterized by regular tetrahedral structures, the absence of Peierls distortion in the crystalline phase, and metavalent bonding [14–16]. The sp^3 gallium hybridization in cubic and amorphous Ga_2Te_3 [16,17] is also different from conventional p-bonding in flagship PCMs, raising questions about its phase-change mechanism. In addition, gallium tellurides exhibit a number of unexpected and highly unusual phenomena, such as nanotectonic compression [15] and viscosity anomalies just above their melting points [18,19]. Nanotectonic compression involves the simultaneous co-crystallization of the stable ambient and metastable high pressure (HP) forms via heating of glassy g-$GaTe_3$ to above the glass transition temperature T_g. The appearance of metallic HP-polymorphs seems to be beneficial for PCM performance because of the resulting higher optical and electric contrast, accompanied by lower power consumption and the possibility of multilevel writing [16]. The viscosity anomaly for several Ga-Te melts in the vicinity of a sesquitelluride composition [18,19] appears to be more significant than the observed "double kink" in liquid germanium tellurides and other PCM alloys [20–23], allowing us to distinguish between two contrasting models: (1) fragile-to-strong transition [20–22] and (2) incipient liquid–liquid immiscibility [23]. Recent high-energy X-ray [24] and neutron diffraction measurements have shown enhanced small-angle scattering below the scattering vector $Q \lesssim 0.4$ Å^{-1}; this is related to the dense metallic liquid droplets in the semiconducting Ga_2Te_3 melt and correlates with non-monotonic viscosity behavior, which can be quantitatively described by the Taylor model [25] for two-phase emulsions. The incipient transient immiscibility within a semiconductor–metal transition in liquid telluride PCMs is an interesting topic for further studies.

The main objectives of the current report are to unravel the atomic structure of amorphous Ga_2Te_5 pulsed laser deposition (PLD) film using high-energy X-ray diffraction, supported by first-principles simulations, and to compare it with the crystal structure of tetragonal gallium pentatelluride [26,27]. The PLD technique is often used for PCM growth, as it provides a stoichiometric transfer from the target to the deposited film and achieves a higher deposition rate [28,29]. In contrast to cubic gallium sesquitelluride Ga_2Te_3, which is a congruently melting compound in the Ga-Te binary system [30–32], tetragonal Ga_2Te_5 is stable over a limited temperature range and exhibits peritectic decomposition before melting. Consequently, the relationship between the amorphous material—obtained by the near instantaneous freezing of the highly excited fragments, particles, liquid globules, etc., existing in the laser-induced plasma (plume)—and a metastable crystal is expected to be complex, leaving room for various intermediate configurations and states. Deep insights into the atomic structure and associated electronic, optical, thermal, and other properties are a key for the rational design of next-generation PCMs and new functional materials for use in photovoltaic, thermoelectric, DNA sensing, and energy storage applications [33–37].

2. Materials and Methods

2.1. Glass and Target Synthesis, Pulsed Laser Deposition

Two different synthesis strategies were applied in efforts to synthesize glassy g-Ga_2Te_5 alloys. First, a small sample (300 mg) of high-purity gallium (99.999%, Neyco) and tellurium (99.999%, Cerac) was prepared in a thin-walled silica tube, which was then sealed under vacuum (10^{-4} mbar) and placed in a rocking furnace. The maximum temperature was 1250 K. The synthesized and homogenized sample was rapidly quenched using a salty ice/water mixture. The crystalline sample was synthesized using fast quenching. Second, a two-step synthesis technique was applied for splat quenching. Crystalline Ga_2Te_5 was prepared as the intermediate step via a conventional melt quenching technique. A tiny piece of the synthesized material was placed into a silica capillary, heated to ≈1050 K, and kept at this temperature for one hour, with subsequent cooling to 950 K. After a supplementary equilibration step for 30 min, the sample was splat-quenched under an argon atmosphere onto a fused silica plate cooled to ≈80 K. A mostly vitreous sample was obtained via splat-quenching.

The gallium pentatelluride target, Ga_2Te_5, for pulsed laser deposition was synthesized in a flat-bottom silica tube with a 25 mm inner diameter. The detailed procedure was described earlier [16], resulting in the final monolithic target with a thickness of 7 mm.

Ga_2Te_5 thin films were deposited at room temperature via PLD onto LCD-grade float glass substrates (Kintec Company, Hong Kong) with a substrate diameter of 2" and a thickness of 1.1 mm. A Neocera PLD system equipped with a 248 nm KrF excimer laser (Coherent Compex 102 F) was used for thin film deposition. The laser beam was focused on a ≈5 mm^2 spot on the surface of the rotating target. The target-to-substrate distance was set at 9 cm, and the pressure in the vacuum chamber was around 3×10^{-6} mbar with no background gas pressure. For the preparation of "thick" layers with a thickness of ≈2 μm, 140,000 laser pulses of 200 mJ pulse energy and 10 Hz repetition rate were used. On the other hand, the "thin" layers with a thickness of ≈100 nm were prepared using 7000 laser pulses of 200 mJ pulse energy and 10 Hz repetition rate. A detailed PLD procedure was reported previously [16,38]. The chemical composition of the PLD films was verified via energy dispersive X-ray spectroscopy and found to be consistent with the target composition: 29.3 ± 0.6 at.% Ga and 70.7 ± 2.0 at.% Te.

2.2. XRD and DSC Characterization

In situ XRD measurements of a Ga_2Te_5 PLD film as a function of temperature have been carried out using a Rigaku Ultima IV diffractometer equipped with a Rigaku SHT-1500 high-temperature platinum camera and sealed Co Kα X-ray tube. The sample was cut from the PLD film on the glass substrate and had dimensions of 9 × 18 mm. The heating rate was 10 K min^{-1} in nitrogen atmosphere. The temperature range was 443 to 653 K with a step of 10 K. After temperature measurements and cooling down the sample, the diffraction pattern was recorded again under ambient conditions. Room-temperature XRD experiments have also been carried out using a Bruker D8 Advance diffractometer (the Cu Kα incident radiation) equipped with a LinxEye detector.

A PLD film powder, removed from the substrate, was used for DSC measurements employing a high precision Netzsch DSC 204 F1 Phoenix instrument (Germany) with μ-sensor. A standard aluminum pan was used for the experiments with a typical heating rate of 10 K min^{-1}.

2.3. Optical and Electrical Measurements

Optical absorption measurements have been carried out over a wide spectral region from 700 nm to 6 μm. A Shimadzu UV-3600 spectrophotometer was used for experiments in the wavelength range of 700–3200 nm. To cover the far-IR region, a Bruker Tensor FTIR spectrometer was used with the extended IR range up to 25 μm. However, the range was limited by 6 μm due to phonon absorption in the glass substrate. The two instruments had overlapping spectral domains in the range of 2.5 and 3.2 μm.

The electrical conductivity of the samples was measured employing a Hewlett Packard 4194A impedance meter over a frequency range of 100 Hz to 15 MHz. The sample resistance was determined by analyzing the complex impedance plots and was then converted into electrical conductivity using the geometrical factor. Further experimental details can be found elsewhere [15].

2.4. High-Energy X-ray Diffraction Measurements

The 6-ID-D beamline at the Advanced Photon Source (Argonne National Laboratory, Chicago, IL, USA) was used for high-energy X-ray diffraction measurements in the top-up mode. The photon energy was 99.9593 keV, and the wavelength was 0.124035 Å. A two-dimensional (2D) setup was used for data collection with a Varex area detector, 2880 × 2880 pixels, and a pixel size of 150 × 150 $μm^2$. The sample-to-detector distance was 302.5 mm. A Ga_2Te_5 PLD film powder, removed from the substrate, was placed into a silica capillary, which was fixed using a sample holder of the instrument. Cerium dioxide CeO_2 was used as a calibrant. The 2D diffraction patterns were reduced using the Fit2D

software [39]. The measured background intensity of the empty capillary was subtracted, and corrections were made for the different detector geometries and efficiencies, sample self-attenuation, and Compton scattering applying standard procedures [40], providing the X-ray structure factor $S_X(Q)$:

$$S_X(Q) = w_{GaGa}(Q)S_{GaGa}(Q) + w_{GaTe}(Q)S_{GaTe}(Q) + w_{TeTe}(Q)S_{TeTe}(Q), \quad (1)$$

where $w_{ij}(Q)$ represents Q-dependent X-ray weighting coefficients and $S_{ij}(Q)$ represents the Faber–Ziman partial structure factors.

2.5. First-Principles Simulation Details

The Born–Oppenheimer molecular dynamics implemented within the CP2K package [41] was used for the modeling of the diffraction data. The generalized gradient approximation (GGA) and the PBE0 hybrid exchange–correlation functional [42,43] combining the exact Hartree–Fock and DFT approaches were used, providing better agreement with experiments [15,16,38,44–46]. The van der Waals dispersion corrections [47] were also employed, improving first-principles molecular dynamics (FPMD) results for telluride systems [48,49]. The applied FPMD technique was similar to previous reports [44–46]. The initial atomic configurations for amorphous Ga_2Te_5 were created and optimized using the RMC_POT++ code [50] in comparison with the experimental $S_X(Q)$. The cubic simulation box, containing 210 atoms (60 Ga and 150 Te), has a size matching the experimental density. Further optimization was carried out using DFT, applying the molecularly optimized correlation consistent polarized triple-zeta valence basis set along with the norm-conserving relativistic Goedecker–Teter–Hutter-type pseudopotentials [51]. FPMD simulations were performed using a canonical NVT ensemble employing a Nosé–Hoover thermostat [52,53]. The simulation boxes were heated from 300 K to 1500 K using 100 K steps for 20–25 ps each. At the highest temperature, the systems were equilibrated for 30 ps and cooled down to 300 K using the same temperature steps but with a longer simulation time (25–30 ps). Final equilibration and data collection at 300 K were performed for 34 ps. The connectivity and ring statistics were analyzed using the R. I. N. G. S. package [54] and a modified connectivity program [55]. The pyMolDyn code [56] was used for the calculation of microscopic voids and cavities.

3. Thermal Properties and Crystallization on Heating

The obtained Ga_2Te_5 PLD thin films were found to be amorphous and vitreous according to XRD and DSC measurements. Typical DSC traces of Ga_2Te_5 PLD and bulk glassy g-$GaTe_3$ are shown in Figure 1e. The endothermic glass transition temperature T_g increases with the gallium content from 448 K (g-$GaTe_3$, 25 at.% Ga) to 491 K (g-Ga_2Te_5, 28.57 at.%). This increase is accompanied by exothermic crystallization. Bulk g-$GaTe_3$ shows two intense thermal features, peaking at 492 and 602 K, along with a very weak intermediate effect at 547 K. The 492 K peak corresponds to primary Te crystallization, presenting both the usual trigonal $P3_12$ and high-pressure monoclinic $P2_1$ forms. On the other hand, the 602 K feature is associated with the formation of cubic ($F\bar{4}3m$) and high-pressure rhombohedral ($R\bar{3}m$) Ga_2Te_3, indicating the occurrence of nanotectonic contraction in a viscous supercooled liquid [15].

In contrast, g-Ga_2Te_5 PLD film shows a single narrow and intense exothermic effect peaking at 545 K with a crystallization onset at $T_x \approx 535$ K. The in situ XRD measurements with a typical DSC heating rate of 10 K min^{-1} were used to reveal the nature of crystallizing phase(s). Surprisingly, the first weak Bragg peaks at the scattering angles $2\theta = 30.5^\circ$ and 63.2° (the Co K_α incident radiation) have appeared just in the vicinity of T_g at ≈483 K, Figure 1a. They correspond to the (002) and (042) reflections of tetragonal Ga_2Te_5, $I4/m$ [26], which was reported to be stable only between 673 and 768 K, Figure 1d. These unexpected results suggest the existence of certain Ga_2Te_5 motifs in the vitreous PLD film evolving into nano-crystallites on heating in a viscous supercooled liquid. Further crystallization advances in the vicinity of T_x when the remaining Bragg peaks of tetragonal Ga_2Te_5 become

visible and grow over the $513 \lesssim T \lesssim 653$ K temperature range, Figure 1b. In addition to the majority gallium pentatelluride $I4/m$ polymorph, trigonal tellurium, $P3_12$ [57], was also detected as a minority phase, Figure 1c,f. Even after cooling the crystallized sample, the observed phases remain intact, specifically retaining the tetragonal Ga_2Te_5, which is metastable at room temperature.

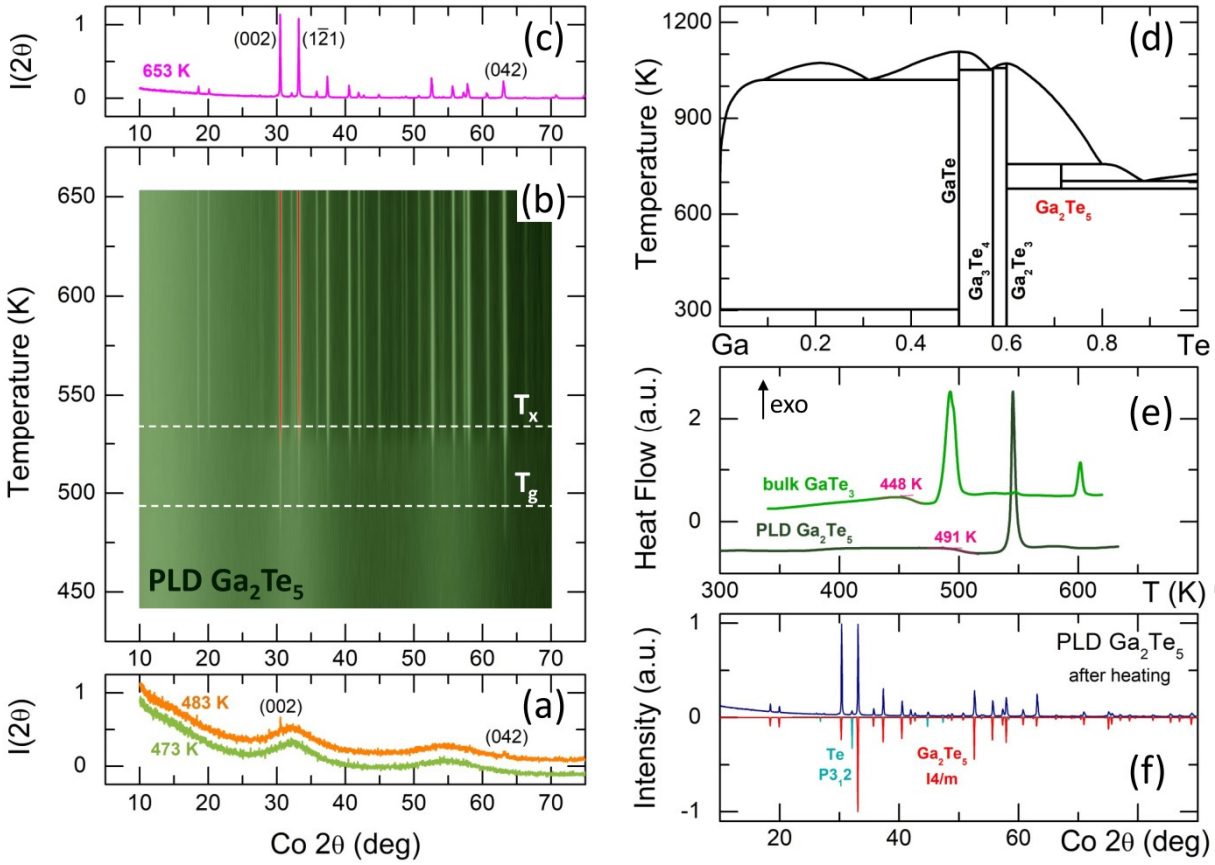

Figure 1. Thermal properties of Ga_2Te_5 PLD films and crystallization on heating. In situ diffraction measurements (**a**) at 473 and 483 K, (**b**) between 443 and 653 K, (**c**) at 653 K; (**d**) Ga−Te phase diagram [30–32]; (**e**) typical DSC traces for Ga_2Te_5 PLD and bulk glassy g−$GaTe_3$, and the glass transition temperatures are also indicated; (**f**) identification of the crystallized phases in Ga_2Te_5 PLD film after cooling from 653 K to room temperature. Trigonal tellurium, $P3_12$ [57], and tetragonal Ga_2Te_5, $I4/m$ [26], were found.

Even more surprisingly, gallium pentatelluride appears to be perfectly stable after 15 months at room temperature, Figure S1 (Supplementary Information), in contrast to bulk Ga_2Te_5, transforming into cubic Ga_2Te_3 and trigonal tellurium within several weeks [30]. In other words, a controlled crystallization of the amorphous Ga_2Te_5 PLD film yields a high-quality, stable tetragonal crystal promising for photovoltaic, thermoelectric, energy storage, and memory applications [33–37]. On the contrary, the slow cooling or fast quenching of molten Ga_2Te_5 gives a polycrystalline mixture of cubic gallium sesquitelluride and trigonal Te, Figure S1, fully consistent with the Ga-Te phase diagram, Figure 1d.

4. Electric and Optical Properties

The measured electrical conductivity of bulk crystalline Ga_2Te_5 is shown in Figure 2a. In contrast to previously reported results [58], the electrical conductivity follows the Arrhenius relationship over the entire temperature range

$$\sigma = \sigma_0 \exp(-E_a/k_B T), \quad (2)$$

where σ_0 is the pre-exponential factor, E_a is the conductivity activation energy, and k_B and T have their usual meanings. Nevertheless, the derived activation energy $E_a = 0.227 \pm 0.003$ eV is identical to that for intrinsic conductivity in tetragonal single-crystal Ga_2Te_5, measured in the direction perpendicular to the *c*-axis [58]. The conductivity pre-factor, $\sigma_0 = 17 \pm 3$ S cm^{-1}, was situated at the lower limit of the electronic transport regime over the extended states [59]. This indicates that $2E_a = 0.45$ eV is approximately the electrical bandgap.

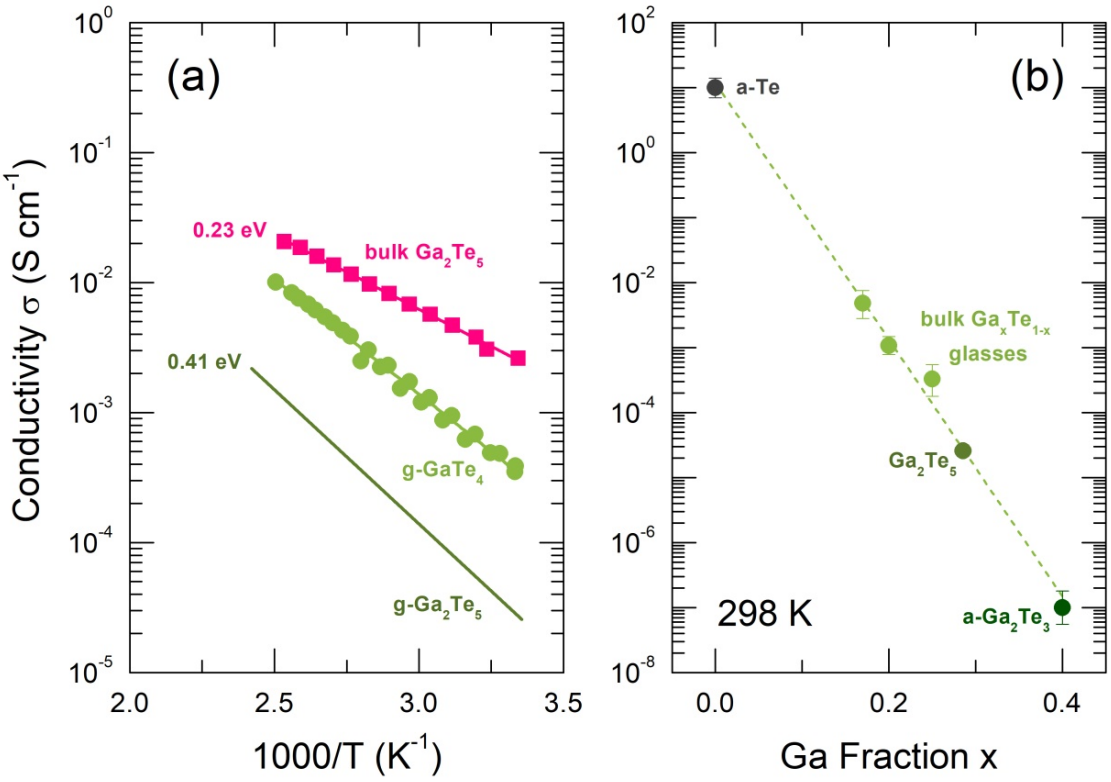

Figure 2. Electrical properties of Ga_xTe_{1-x} amorphous, glassy, and crystalline materials: (**a**) electrical conductivity of bulk crystalline Ga_2Te_5 (this work), bulk glassy g−$GaTe_4$ [15], and interpolated conductivity for g−Ga_2Te_5, and the derived activation energies E_a are also indicated; (**b**) room-temperature conductivity for amorphous a−Te thin film, corresponding to band-to-band electronic transport [60], bulk Ga−Te glasses [15], and amorphous a−Ga_2Te_3 [61]; the interpolated value for g−Ga_2Te_5 is also shown.

The electrical conductivity for glassy g-Ga_2Te_5 was obtained via the interpolation of the available data for amorphous and glassy Ga_xTe_{1-x} alloys, where $0 \leq x \leq 0.4$ [15,60,61], as shown in Figure 2b. The room-temperature conductivity appears to be a decreasing exponential function of the gallium content x:

$$\sigma_{298}(x) = \sigma_{298}(0)\exp(ax)\,, \tag{3}$$

where $\sigma_{298}(0)$ is the conductivity of amorphous Te and $a < 0$ is a constant. In other words, the electronic conductivity of disordered Ga-Te materials primarily relies on the tellurium concentration. The interpolated g-Ga_2Te_5 conductivity is lower by two orders of magnitude compared to the σ_{298} value of bulk crystalline pentatelluride. The estimated conductivity activation energy, $E_a = 0.41$ eV, and the pre-exponential factor, $\sigma_0 \approx 220$ S cm^{-1}, suggest the electrical bandgap of the glassy polymorph is about 0.8 eV.

Figure 3 shows the optical properties of Ga_2Te_5 PLD films. The absorption measurements reveal a fundamental optical absorption edge below the incident wavelength $\lambda \lesssim 1.2$ μm accompanied by distinct interference fringes. These fringes indicate a homogeneous nature and uniform thickness of the PLD film. The observed fringes allow both the

refractive index n_R and the film thickness to be calculated using the Swanepoel method [62]. Moreover, due to the well-defined interference across the spectral range and the considerable thickness of the PLD film (2.7 μm), it also becomes possible to estimate the refractive index dispersion $n_R(\lambda)$.

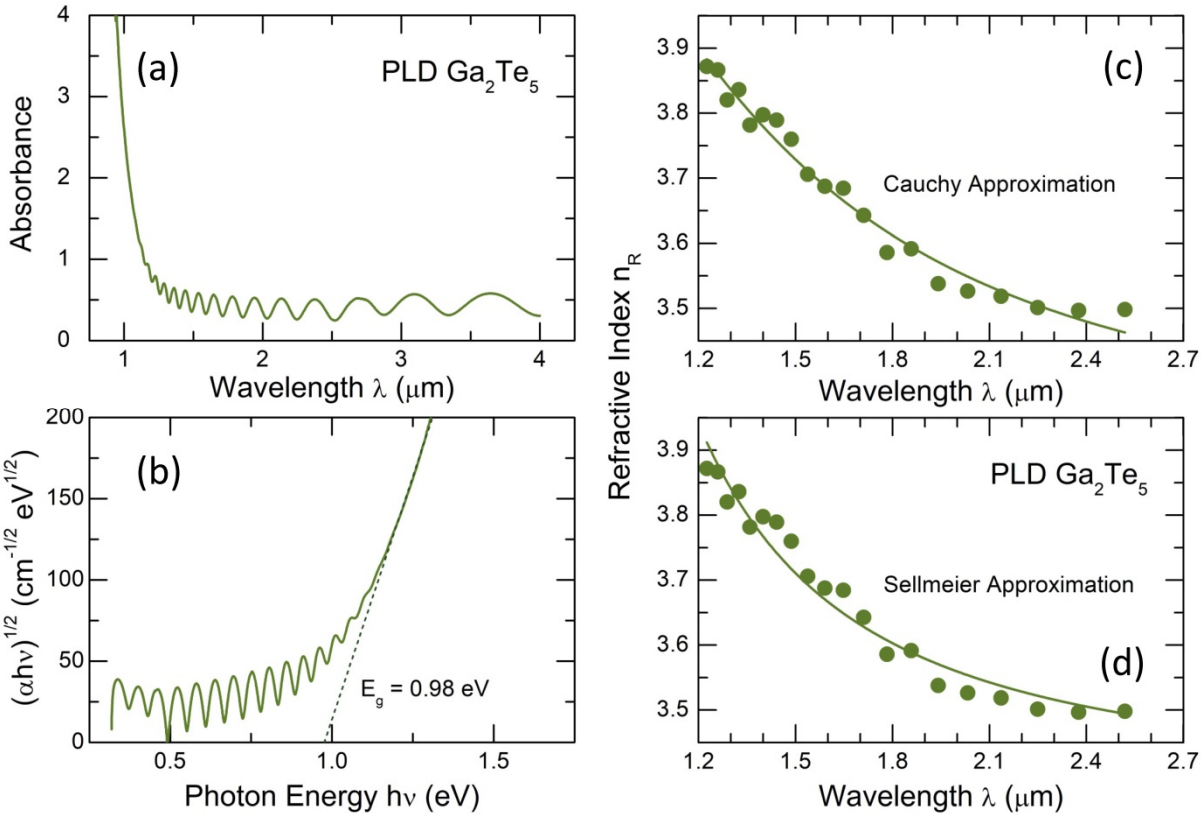

Figure 3. Optical properties of Ga_2Te_5 PLD films: (**a**) optical absorbance with interference fringes as a function of the incident wavelength λ; (**b**) the Tauc plot, $\sqrt{\alpha h\nu}$ vs. photon energy $h\nu$, where α is the absorption coefficient, yielding the optical band gap E_g; (**c**) the Cauchy and (**d**) Sellmeier approximations [63] describing the dispersion of the refractive index n_R as a function of λ. See the text for further details.

Two approaches are usually applied to represent the refractive index dispersion [63]. The Cauchy approximation of the derived data $n_R(\lambda)$ is given in Figure 3c, as follows:

$$n_R(\lambda) = A + \frac{B}{\lambda^2} + \frac{C}{\lambda^4}, \tag{4}$$

where A, B, and C are constants which are characteristic of any given material. Since the Cauchy equation is inappropriate in a region of anomalous dispersion [63], the Sellmeier approach is often used, considering the existence in an optical material of dipole oscillators with a resonance frequency v_0:

$$n_R(\lambda)^2 = 1 + \frac{A\lambda^2}{\lambda^2 - \lambda_0^2}, \tag{5}$$

where A and $\lambda_0 = c/v_0$ are two characteristic constants, and c is the speed of light. Usually, the Sellmeier equation is written with a series of terms to account for different resonance frequencies over an extended domain, that is, v_0, v_1, etc.:

$$n_R(\lambda)^2 = 1 + \frac{A_0\lambda^2}{\lambda^2 - \lambda_0^2} + \frac{A_1\lambda^2}{\lambda^2 - \lambda_1^2} + \ldots \tag{6}$$

The Sellmeier coefficients A_i and λ_i allow the normal dispersion of optical glasses to be calculated over a wide spectral range. In our case, we were limited to the original Sellmeier equation (5) with the following coefficients: A_0 = 3.5017 and λ_0 = 0.3992 (Figure 3d). Due to an insufficient spectral range and experimental uncertainty, the higher-order terms in the refractive index dispersion could not be accessed. Nevertheless, despite this limitation, the two approaches describe the derived $n_R(\lambda)$ values reasonably well.

The optical absorption results were also used to calculate the optical bandgap E_g applying the Tauc relation [64]:

$$\alpha = \frac{A(h\nu - E_g)^2}{h\nu}, \tag{7}$$

where α is the absorption coefficient, $h\nu$ the photon energy, and $A \approx 10^5$ cm^{-1} eV^{-1} is a constant.

As expected, the derived bandgap E_g = 0.98 ± 0.02 eV, Figure 3b, for glassy gallium pentatelluride was found to be smaller than that for g-Ga_2Te_3, which was 1.20 eV [16], supporting the predominant role of the tellurium content on electronic and optical properties of Ga-Te alloys. Simultaneously, the optical E_g appears to be comparable with the electrical counterpart, $2E_a$ = 0.82 eV.

The thermally annealed and crystallized Ga_2Te_5 PLD film exhibits more complicated optical absorption, Figure 4. The absorbance below $\lambda \lesssim 1$ μm shows a distinct blue-shift, while the low-energy absorbance becomes more intense and mostly loses interference fringes indicating less homogeneous material in both the chemical composition and thickness. Taking into account the presence of (nano)crystallites in the annealed PLD film, additional scattering corrections were applied simultaneously with the usual reflection corrections. The refractive index $n_R(\lambda)$ of g-Ga_2Te_5 was used for these calculations.

The Mie theory of light scattering for turbidity τ measurements and the wavelength exponent $\lambda^{-\chi}$ were employed for the scattering corrections [65,66]:

$$\tau = l^{-1} \ln(I_0/I), \tag{8}$$

where l is the scattering path length, and I_0 and I are the intensities of the incident and transmitted beam, respectively. The turbidity depends on several parameters:

$$\tau = B_s N_p V_p^2 \lambda^{-\chi}, \tag{9}$$

where B_s is the scattering coefficient, N_p is the particle number density, V_p is the average volume of the particle, and χ is the wavelength exponent. Combining Equations (8) and (9), one obtains

$$D = K_s \lambda^{-\chi} \tag{10}$$

where $D = \log(I_0/I)$ is the optical density and K_s is a constant. The values of K_s and χ were obtained by plotting $\ln D$ vs. $\ln \lambda$ (Figure S2), which allows both the turbidity $\tau(\lambda)$ and χ to be determined and the scattering corrections to be calculated. The theoretical Heller wavelength exponent χ_0 [65] yields the average particle size $\langle r_p \rangle$, which was found to be $\langle r_p \rangle \approx 110$ nm for c-Ga_2Te_5, Figure S2. The derived $\langle r_p \rangle$ value is consistent with the size of crystallites, obtained from the XRD linewidth Γ, yielding $\left\langle r_p^{XRD} \right\rangle = 2\pi/\Gamma > 50$ nm. The final absorbance corrected for reflection and scattering is shown in Figure 4a.

The derived optical absorption coefficient α, presented in Figure 4b, exhibits two optical processes above and below the incident photon energy $h\nu \approx 1.3$ eV. Basically, the overall shape of the absorption coefficient α is reminiscent of the behavior observed in materials such as silicon or carbon [67,68]. This shape is typically associated with direct

optical transition at higher photon energies $h\nu$ and indirect optical absorption at lower $h\nu$ [68–72]. Assuming direct optical transition in crystallized Ga_2Te_5 above 1.3 eV,

$$\alpha h\nu = A\left(h\nu - E_g^d\right)^{1/2}, \tag{11}$$

the direct optical bandgap was found to be $E_g^d = 1.36 \pm 0.03$ eV, Figure 4c. The constant A in Equation (11) is given by $A \approx \left[e^2/\left(n_R c h^2 m_e^*\right)\right](2m^*)^{3/2}$, where e is the electron charge and m^* is a reduced electron and hole effective mass [69].

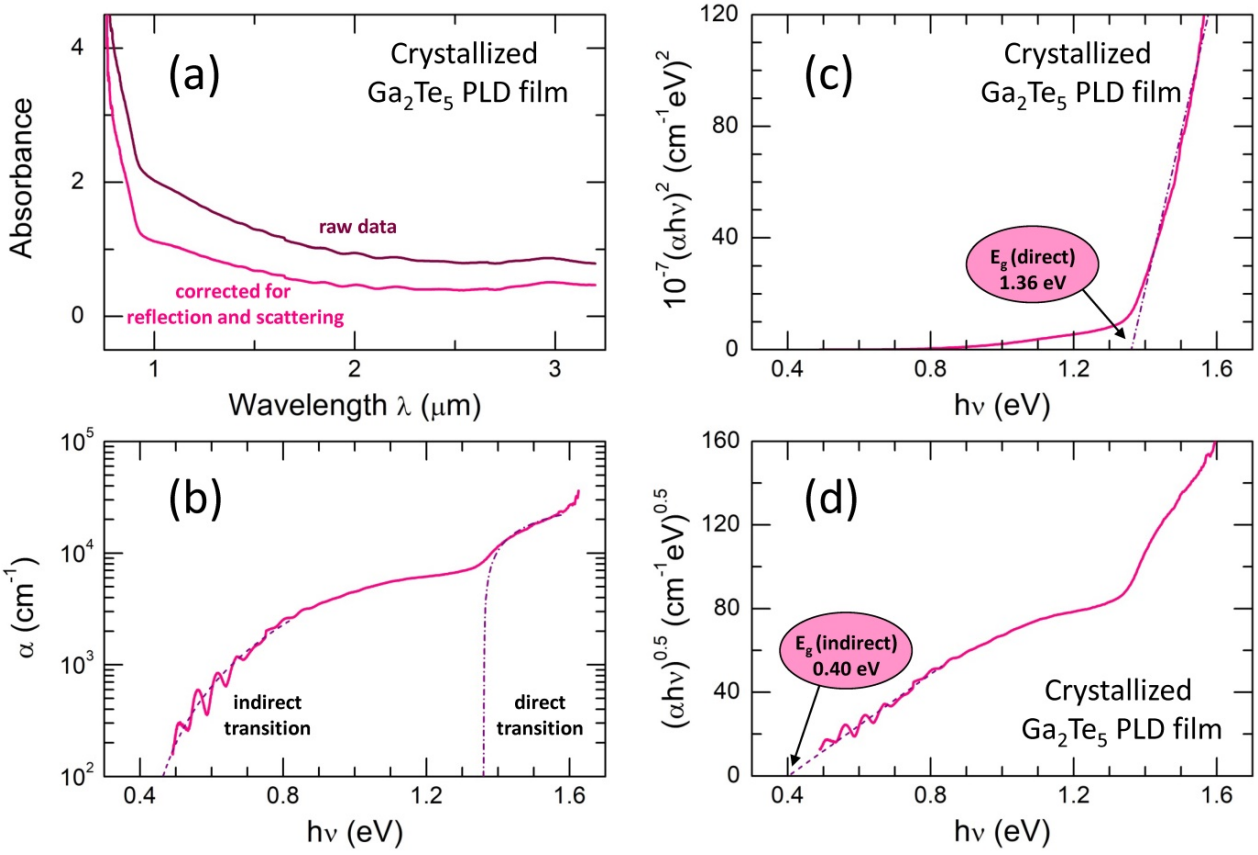

Figure 4. Optical properties of crystallized Ga_2Te_5 PLD film: (**a**) raw absorbance data and absorbance corrected for reflection and scattering; (**b**) absorption coefficient α and the analysis results for direct (the dash-dotted line) and indirect (the dashed line) optical transitions; (**c**) data analysis suggesting direct optical transition; the derived direct optical gap E_g^d is also indicated; (**d**) data analysis assuming indirect optical transition; the derived indirect optical gap E_g^i is indicated. See the text for further details.

The optical absorption plotted as $\sqrt{\alpha h\nu}$ vs. photon energy $h\nu$, Equation (7), yields the indirect optical bandgap $E_g^i = 0.40 \pm 0.03$ eV, Figure 4d. The derived value is consistent with the electrical bandgap of c-Ga_2Te_5, $2E_a = 0.45$ eV, Figure 2a.

The experimental data for tetragonal Ga_2Te_5, obtained using the conductivity and Hall effect measurements, are strongly anisotropic and changing over a wide range between 0.46 and 1.79 eV [58]. The calculated E_g values are also variable, $0.86 \leq E_g \leq 1.7$ eV [72,73], depending on the applied simulation method. Nevertheless, the results of electrical and optical measurements show a reasonable contrast between amorphous (SET) and crystalline (RESET) states for Ga_2Te_5.

5. High-Energy X-Ray Diffraction

The high-energy X-ray diffraction data in Q-space are shown in Figure 5. In contrast to fast cooled Ga_2Te_5 in a thin-walled silica tube, mostly consisting of cubic Ga_2Te_3 and trigo-

nal tellurium with some vitreous fraction (Figure S1), the splat-quenching of tiny Ga_2Te_5 droplets yields an essentially glassy material. However, this glassy material is accompanied by non-negligible nanocrystals of cubic gallium sesquisulfide, as seen in Figure 5a. The spontaneous Ga_2Te_3 crystallization is consistent with the Ga-Te phase diagram, Figure 1d, related to peritectic decomposition of Ga_2Te_5 above 768 K. The obtained Ga_2Te_5 PLD films are fully vitreous with a distinct glass transition temperature at 491 K, Figure 1e. The X-ray structure factor $S_X(Q)$ of g-Ga_2Te_5 PLD appears to be intermediate between bulk glassy $GaTe_4$ and Ga_2Te_3 PLD film, Figure 5b, suggesting structural similarities and revealing a systematic evolution of vitreous Ga_xTe_{1-x} materials with increasing gallium content x independently of preparation techniques.

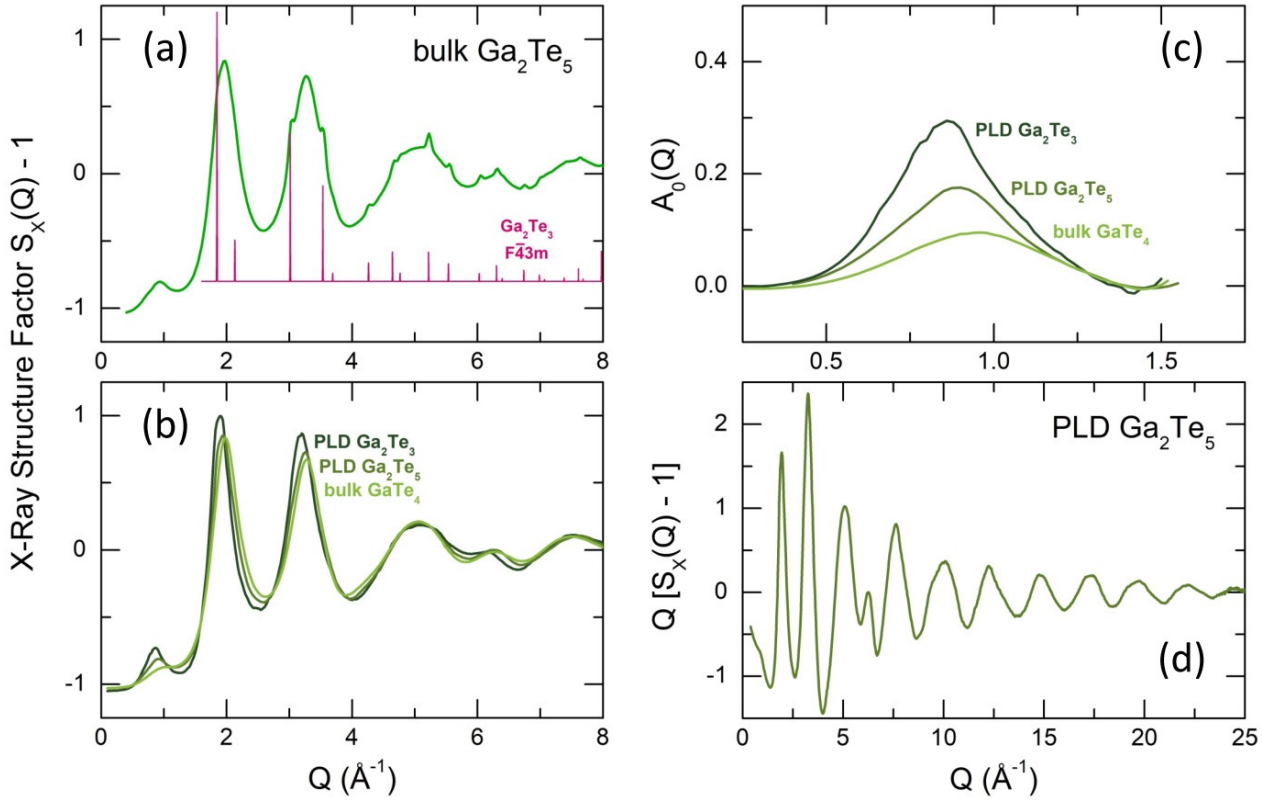

Figure 5. Diffraction data in Q-space: the X-ray structure factor $S_X(Q)$ of (**a**) bulk splat-quenched Ga_2Te_5 and (**b**) Ga_2Te_3, Ga_2Te_5 PLD films and bulk glassy g$-GaTe_4$ over a limited Q -range; (**c**) isolated first sharp diffraction peaks (FSDP) for Ga_2Te_3 and Ga_2Te_5 PLD films and g$-GaTe_4$; (**d**) the interference function $Q[S_X(Q) - 1]$ for Ga_2Te_5 PLD film over the extended Q $-$range. The Bragg peaks for cubic Ga_2Te_3 (space group $F\bar{4}3m$) are also shown in (**a**).

In particular, we observe an emerging and growing first sharp diffraction peak (FSDP), also shifting to a lower Q with increasing x from $Q_0 = 0.94 \pm 0.01$ Å^{-1} ($GaTe_4$, $x = 0.2$) to 0.86 ± 0.01 Å^{-1} (Ga_2Te_3, $x = 0.4$), Figure 5c. The isolated FSDPs were obtained using the subtraction procedure [74,75]. The FSDP systematics (position Q_0 and amplitude A_0) reveals monotonic and nearly linear trends as a function of x, Figure S3, for both bulk glasses ($0.17 \leq x \leq 0.25$) and vitreous PLD films ($0.2857 \leq x \leq 0.40$). The observed trends suggest that there are structural similarities on the short- and intermediate-range scale.

Distinct high-Q oscillations, clearly visible over the extended Q-range for the Ga_2Te_5 interference function $Q[S_X(Q) - 1]$, Figure 5d, enable high real-space resolution for atomic pair distribution $g_X(r)$ and total correlation $T_X(r)$ functions after the usual Fourier transform:

$$T_X(r) = 4\pi\rho_0 r + \frac{2}{\pi}\int_0^{Q_{max}} Q[S_X(Q) - 1]\sin QrM(Q)\mathrm{d}Q, \quad (12)$$

where ρ_0 is the experimental number density, $M(Q)$ the Lorch window function, and Q_{max} = 30 Å^{-1}.

The derived $T_X(r)$ for g-Ga_2Te_5 PLD film is shown in Figure 6. The asymmetric feature between 2.4 and 3.2 Å corresponds to Ga-Te and Te-Te nearest neighbors (NN). Gaussian fitting of the experimental data (Table 1) yields tetrahedral gallium coordination at a distance of 2.64 Å, consistent with the known Ga-Te coordination numbers and NN distances in crystalline and glassy gallium tellurides [14–16,26,27,30,76–78]. On the contrary, the Te-Te atomic pairs in glassy Ga_2Te_5 are markedly shorter (2.80 Å) than those in tetragonal gallium pentatelluride (3.027 Å) [26]. Nevertheless, the Te-Te NN distance of 2.80 Å is typical for amorphous and trigonal tellurium [57,79] and Te-rich binary and ternary glasses [15,77,78,80]. The partial $T_{ij}(r)$ correlation functions for tetragonal gallium pentatelluride are compared in Figure 6b with an experimental $T_X(r)$ for g-Ga_2Te_5. We note both similarities and differences for the two materials.

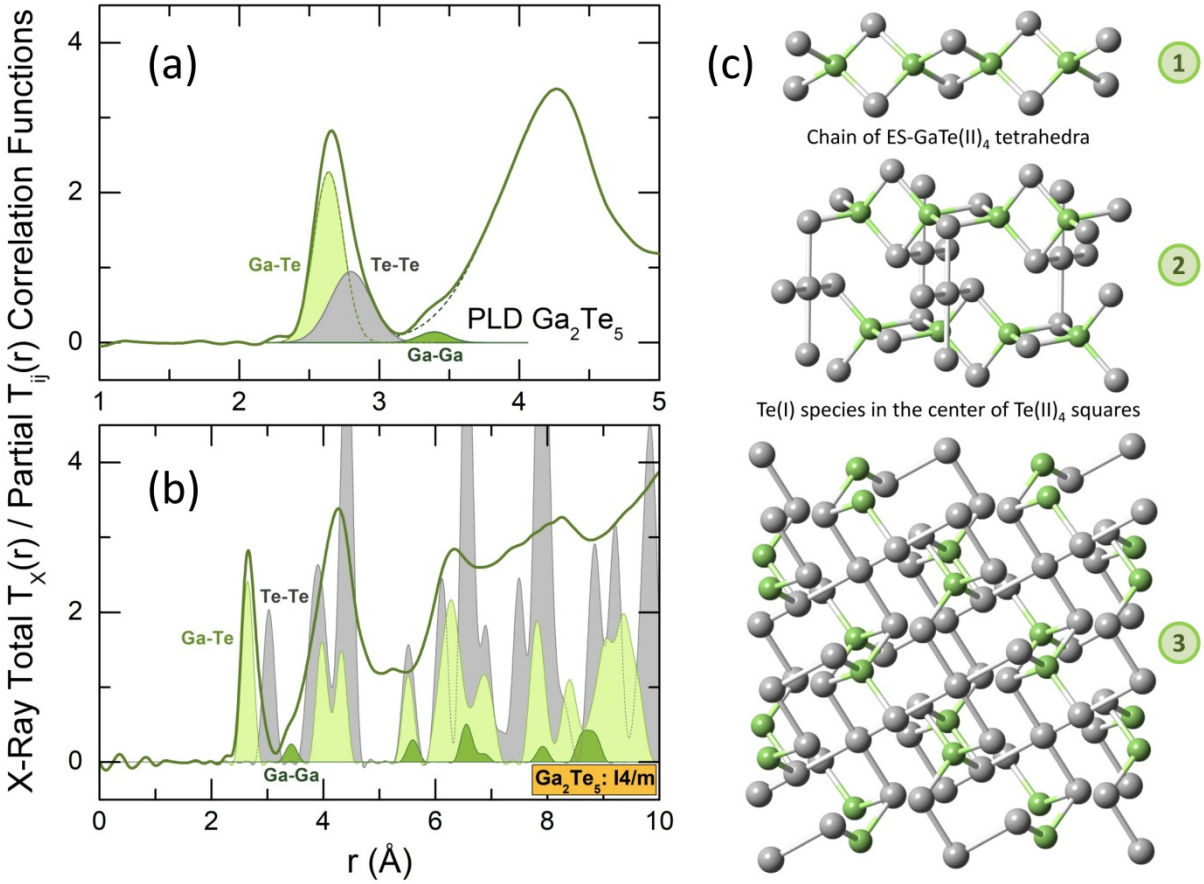

Figure 6. Diffraction data in *r*-space: the X-ray total correlation function $T_X(r)$ for g-Ga_2Te_5 PLD film, showing (**a**) a four-peak Gaussian fitting of the nearest (NN) and second (2N) neighbor features between 2.4 and 4.5 Å; the Ga-Te and Te-Te NNs are highlighted in light green and gray, respectively; the Ga-Ga 2Ns are green; (**b**) a comparison with the partial correlation functions $T_{ij}(r)$ for tetragonal Ga_2Te_5 (space group $I4/m$ [26]), derived using the XTAL code [76]; (**c**) the crystal structure of tetragonal gallium pentatelluride, revealing (1) infinite chain of edge-sharing ES-GaTe(II)$_4$ tetrahedra along the *c* -axis, (2) two neighboring chains connected by Te(I) species located in the center of Te(II) squares, (3) an approximate (**a**, **b**) projection of the crystal structure.

The crystalline counterpart is stable over a narrow temperature range from 673 to 768 K [30–32], as shown in Figure 1d. In contrast to layered compounds like Al_2Te_5 and In_2Te_5 [27], gallium pentatelluride has a 3D structure consisting of infinite chains, parallel to the *c* axis. The chains are formed by edge-sharing ES-GaTe(II)$_4$ tetrahedra, Figure 6c.

Additionally, every four ES-GaTe(II)$_4$ entities from neighboring chains are linked together by Te(I) species, located at the center of squares, formed by Te(II).

Table 1. Interatomic distances r_{ij} and partial coordination numbers N_{ij} of the nearest neighbors in glassy Ga_2Te_5 PLD films according to high-energy X-ray diffraction and first-principles molecular dynamics.

Ga-Ga		Ga-Te		Te-Te		N_{Ga-X}
r_{ij} (Å)	N_{ij}	r_{ij} (Å)	N_{ij}	r_{ij} (Å)	N_{ij}	
High-energy X-ray diffraction						
-	-	2.637(3)	3.98(5)	2.796(5)	1.01(8)	3.98(5)
First-principles molecular dynamics (GGA/PBE0)						
2.417	0.03	2.615 *	3.97	2.802 *	0.93	4.00

* asymmetric peak.

These square-planar Te_5 units (crosses) are mostly absent in glassy Ga_2Te_5, as evidenced by the significantly lower Te-Te NN coordination number, N^{PLD}_{Te-Te} = 1.01 ± 0.08 (Table 1), compared to the crystal counterpart, $N^{I4/m}_{Te-Te}$= 1.6 = $^1/_5 \times 4 + ^4/_5 \times 1$, which represents the average Te-Te coordination for the Te(I) and Te(II) species, Figure 6c. On the other hand, the existence of ES-GaTe$_4$ tetrahedra in the glass network is indicated by the presence of a weak shoulder at 3.39 ± 0.02 Å for the asymmetric second neighbor peak, centered at ≈4.3 Å. The short Ga-Ga second neighbor correlations, characteristic of ES-units in tetragonal Ga_2Te_5, are located at 3.424 Å, Figure 6b. However, due to a weak average Ga-Ga weighting factor, $\langle w^X_{GaGa}(Q)\rangle$ = 0.02964 vs. $\langle w^X_{GaTe}(Q)\rangle$ = 0.28405 or $\langle w^X_{TeTe}(Q)\rangle$ = 0.68630, the amplitude of this feature is small. The weak average Ga-Ga weighting factor, as well as the truncation ripples, related to a finite Q-range of the Fourier transform, enable only a rough estimation of N^{PLD}_{Ga-Ga} = 1.2 ± 0.4, compared to $N^{I4/m}_{Ga-Ga}$ = 2. A deep insight into the atomic structure of vitreous Ga_2Te_5 PLD films yields first-principles molecular dynamics.

6. First-Principles Molecular Dynamics

Simulated FPMD X-ray structure factor $S_X(Q)$ and pair-distribution function $g_X(r)$ for glassy Ga_2Te_5 in comparison with experimental results are shown in Figure 7a,b. We note that the GGA approximation with hybrid PBE0 functional describes the experimental data well, as it was reported earlier [15,16,44–46]. The positions and amplitudes of the diffraction features in both Q- and r-space are reproduced.

The calculated partial structure factors $S_{ij}(Q)$ are displayed in Figure 7c. As expected, the main contribution to the FSDP comes from the Ga-Ga partial $S_{GaGa}(Q)$. The simulated $g_{ij}(r)$, Figure 7d, reveal complicated short- and intermediate-range orders.

The asymmetric Ga-Te NN correlations appear at 2.62 Å and suggest at least two contributions with slightly different bond lengths. The Ga-Te coordination number is consistent with the experiment, N^{FPMD}_{Ga-Te} = 3.97, Table 1, assuming a tetrahedral gallium local environment. In addition to homopolar Te-Te bonds at 2.80 Å, a weak Ga-Ga NN feature at 2.42 Å was also found. The amplitude of this peak is too small to be observed experimentally, Figure 7b. The Ga-Ga second neighbors between 3 and 4.5 Å have a bimodal distribution. The shoulder at ≈3.35 Å indicates the ES-units, while the main contribution at 3.92 Å is related to corner-sharing CS-entities. Consequently, the fraction of ES-GaTe$_4$ in the glassy Ga_2Te_5, f^{FPMD}_{ES} = 0.45, is significantly lower than that in tetragonal polymorph, $f^{I4/m}_{ES}$ = 1, indicating that only ES-GaTe$_4$ are present in the crystalline counterpart. The experimental value, f^{PLD}_{ES} = 0.6 ± 0.2, is reasonably consistent with the FPMD result. Basically, the experimental and FPMD structural parameters were found to be similar or identical, Table 1.

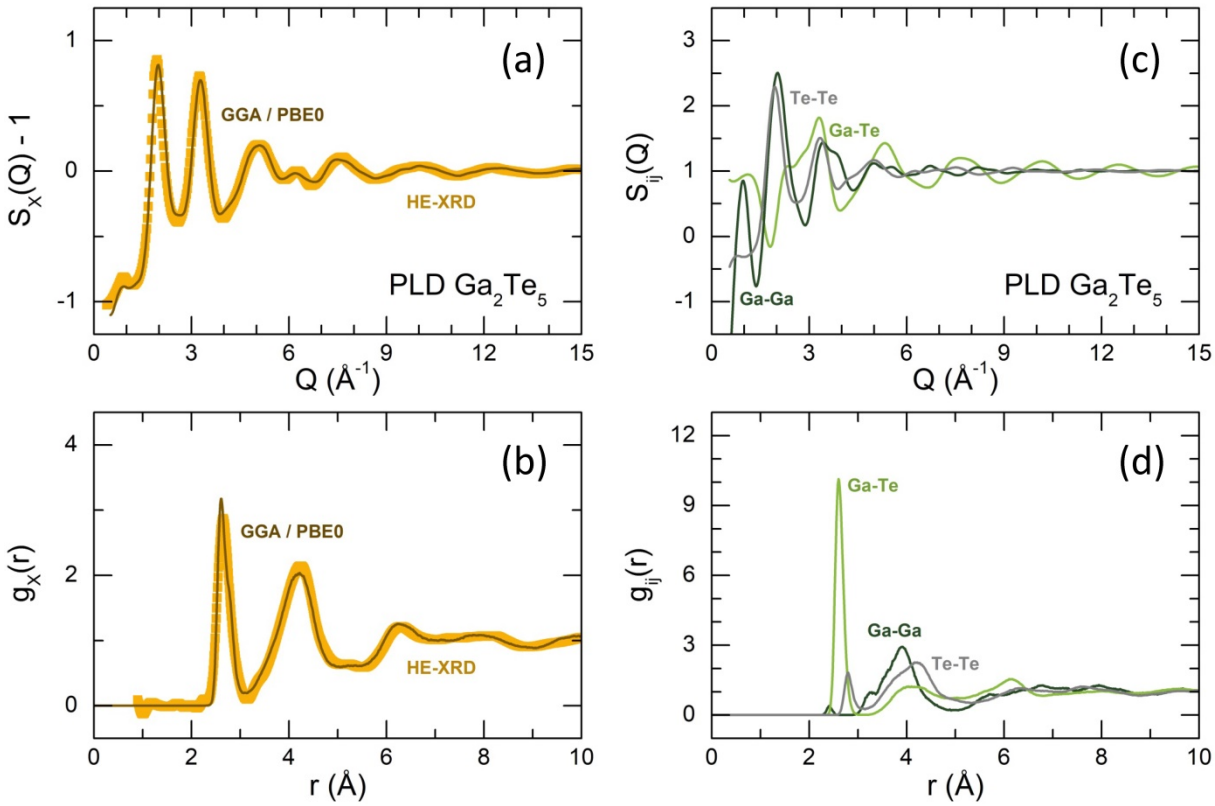

Figure 7. First-principles molecular dynamics modeling of Ga_2Te_5 PLD film using GGA/PBE0 approximation; calculated and experimental (**a**) X-ray structure factors $S_X(Q)$; (**b**) pair-distribution functions $g_X(r)$; (**c**) partial structure factors $S_{ij}(Q)$; (**d**) partial pair distribution functions $g_{ij}(r)$. The Ga−Ga, Ga−Te, and Te−Te partials are dark green, light green, and grey, respectively.

The Ga and Te local coordination distributions are presented in Figure 8. The tetrahedral gallium coordination $Ga(Te_{4-m}Ga_m)$ contains negligible number of Ga-Ga homopolar pairs ($m = 1$). In contrast, tellurium has multiple coordination environments $Te(Ga_{n-m}Te_m)$, $1 \leq n \leq 4$, but only two-fold Te_{2F} (50.5%) and three-fold Te_{3F} (47.6%) coordinated species are the most abundant. The tellurium forms reveal a large variability in Te-Te bonds, $0 \leq m \leq 4$, from pure heteropolar Te-Ga coordination ($m = 0$) to fully homopolar environment ($m = n$). We should, however, note a small fraction of Te_{4F} species (1.87%) and a negligible number of Te_5 square-planar entities (0.23%), the only form of tellurium subnetwork in tetragonal gallium pentatelluride, Figure 6c. This result is coherent with the reduced Te-Te coordination number $N^{PLD}_{Te-Te} \cong N^{FPMD}_{Te-Te} \cong 1$, Table 1.

The geometry of $GaTe_4$ units yields either Te-Ga-Te bond angles or the orientational order parameter q [81,82]. Figure 9a,c show the calculated $B_{TeGaTe}(\theta)/\sin\theta$ bond angle distribution for g-Ga_2Te_5 in comparison with tetragonal Ga_2Te_5 and cubic Ga_2Te_3, respectively. We note a broad and slightly asymmetric $B_{TeGaTe}(\theta)/\sin\theta$ function, centered at 103.3 ± 0.3°, for the PLD film (Figure S4). The Te-Ga-Te angles in the two crystalline references, characterizing both distorted ES-$GaTe_4$ tetrahedra in gallium pentatelluride and regular CS-units in cubic sesquitelluride, are located within the glassy envelope but do not reproduce it via simple broadening. Nevertheless, the tetrahedral geometry in tetragonal Ga_2Te_5 seems to be closer to that in the glass.

The connectivity of $GaTe_4$ tetrahedra is given by the Ga-Te-Ga triplets or the respective $B_{GaTeGa}(\theta)/\sin\theta$ distributions, Figure 9b,d. The difference in connectivity between g-Ga_2Te_5 and the crystalline structures is even more significant but a remote resemblance to the connected ES-entities in the tetragonal crystal still exists.

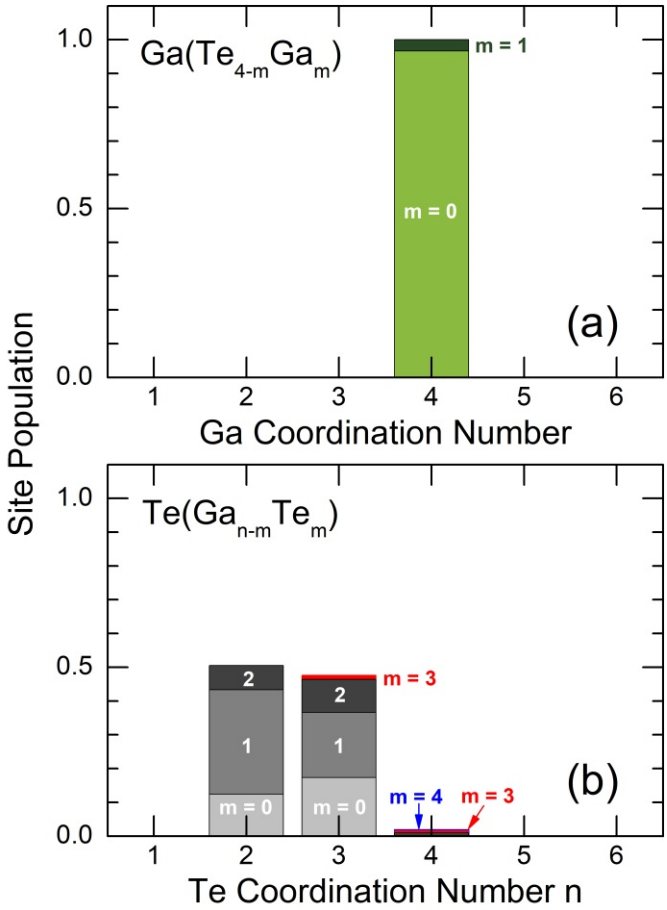

Figure 8. (**a**) Gallium and (**b**) tellurium coordination distributions. Tetrahedral gallium coordination $\mathrm{Ga}(\mathrm{Te}_{4-m}\mathrm{Ga}_m)$ contains a negligible number of Ga-Ga homopolar pairs (m = 1). Multiple tellurium coordination environments $\mathrm{Te}(\mathrm{Ga}_{n-m}\mathrm{Te}_m)$, $1 \leq n \leq 4$, contain a significant number of Te−Te bonds, $0 \leq m \leq 4$. See the text for further details.

The order parameter q [81,82] is often used to evaluate the polyhedral topology and distinguish between tetrahedral and non-tetrahedral local geometry of four-fold coordinated $GaTe_4$ entities

$$q = 1 - \frac{3}{8}\sum_{j=1}^{3}\sum_{k=j+1}^{4}\left(\cos\psi_{jk} + \frac{1}{3}\right)^2, \tag{13}$$

where ψ_{jk} is the Te-Ga-Te angle of the central gallium atom with its nearest Te neighbors j and k. The average value of q changes between 0 for an ideal gas and q = 1 for a regular tetrahedral network. The $P(q)$ probability distribution function is shown in Figure 10a. Asymmetric $P(q)$ is peaked at q = 0.93 and decreases sharply both ways to high and low q. Usually, the tetrahedral limit is set at $q \geq 0.8$ [44,83]. The $P(q)$ integration within these limitations shows that 97% of $GaTe_4$ units belong to the tetrahedral geometry. The remaining entities (3%) are likely defect octahedral species $GaTe_4$ with two missing Te neighbors around the central Ga atom, characterized by $0.4 < q < 0.8$. The regular defect octahedron ($\psi_1 = \pi$ and $\psi_2 = \pi/2$) has $q = 5/8$. The obtained results differ drastically from flagship PCM (GeTe, $Ge_2Sb_2Te_5$), which show a significant fraction of defect octahedral sites and a minority of tetrahedral structural units ($\lesssim$40%) [28,83–87]. The exact proportion varies depending on experimental technique, that is, EXAFS or diffraction, and the exchange–correlation functional for FPMD simulations.

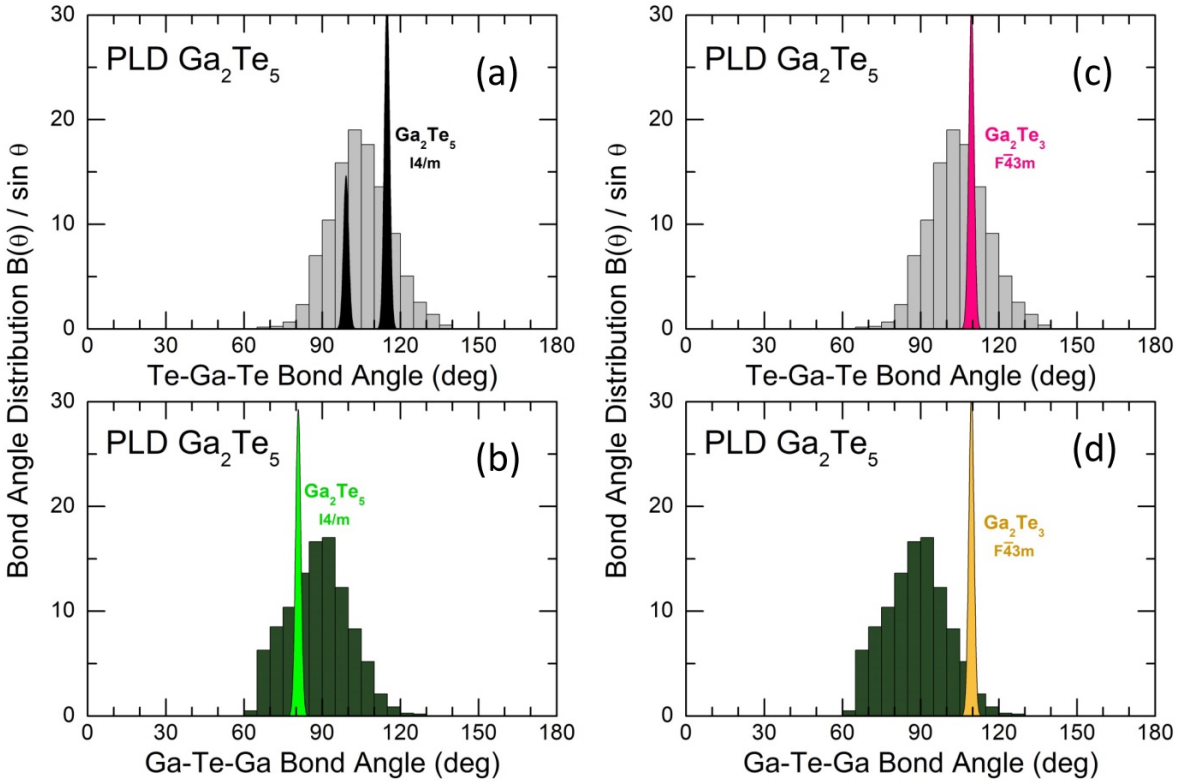

Figure 9. Bond angle distributions $B(\theta)/\sin\theta$ in simulated g-Ga_2Te_5: (**a**,**c**) the Te-Ga-Te and (**b**,**d**) Ga-Te-Ga bond angles in comparison with (**a**,**b**) tetragonal Ga_2Te_5 and (**c**,**d**) cubic Ga_2Te_3.

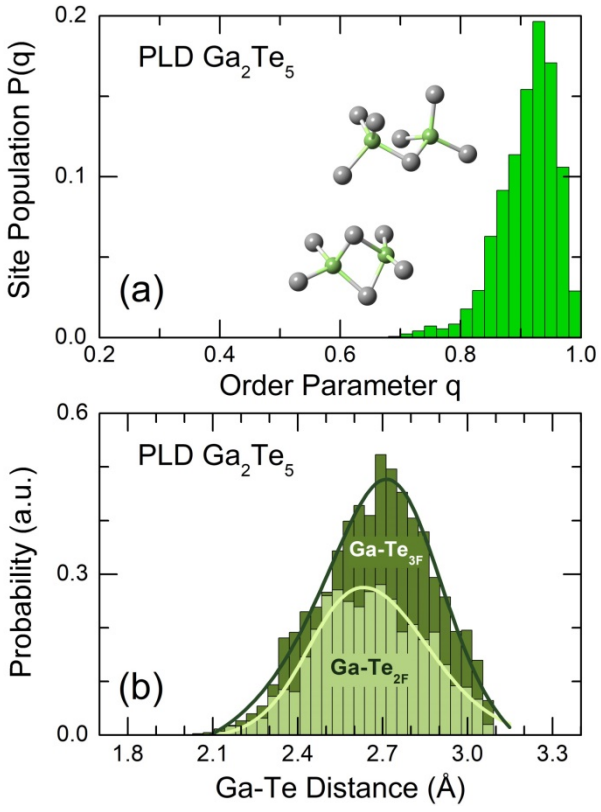

Figure 10. (**a**) Orientational order parameter q [81,82] for 4-fold coordinated Ga species in g-Ga_2Te_5 and (**b**) Ga-Te NN distance distributions for two-fold Te_{2F} and three-fold Te_{3F} coordinated tellurium atoms.

Two-fold and three-fold coordinated tellurium can explain the asymmetric shape of the Ga-Te NN peak. The calculated Ga-Te_{2F} and Ga-Te_{3F} distances are presented in Figure 10b. The two distributions are broad and asymmetric but have slightly different maxima. The Ga-Te_{3F} bonds are longer (a broad maximum at 2.71 ± 0.03 Å) compared to Ga-Te_{2F}, peaked at 2.63 ± 0.02 Å. A similar difference, $\Delta r_{3F-2F} = 0.12 \pm 0.01$ Å, was reported in monoclinic Ga_2S_3 [88] with an ordered distribution of gallium vacancies. The ratio of Ga-Te_{3F} to Ga-Te_{2F} bond populations, $r = [Ga - Te_{3F}]/[Ga - Te_{2F}] = 1.75$, was also found to be similar to the expected stoichiometric ratio $r_0 = 2$ for tetrahedral Ga species, which possess the formal oxidation state Ga^{3+} and correspond to the Ga_2Te_3 alloy composition.

The connectivity analysis shows that all Ga and Te species are connected. The analysis of Te-Te connectivity reveals a different size of Te_k fragments, Figure 11a. Tellurium monomers ($k = 1$), that is, Te atoms with only heteropolar Te-Ga bonds, and dimers ($k = 2$) represent a relative majority, 55%, of all Te_k fragments. The remaining fragments can be divided into two groups: (i) $3 \leq k \leq 6$ (see the inset in Figure 11a) and (ii) oligomeric chains, $k = 15$, for the used 210-atom simulation box. Group (i) represents the remnants of square-planar Te_5 units in tetragonal Ga_2Te_5 (the inset in Figure 11b), also confirmed by bond angle distribution $B_{TeTeTe}(\theta)/\sin\theta$. Group (ii) is similar to chains in trigonal tellurium, $P3_12$ [57], supported by a contribution at about $\theta_{TeTeTe} \approx 103°$, Figure 11b. The presence of two distinct groups is likely a consequence of the limited thermal stability of tetragonal gallium pentatelluride and peritectic reaction $Ga_2Te_5 \rightleftarrows Ga_2Te_3 + 2Te$ above 768 K.

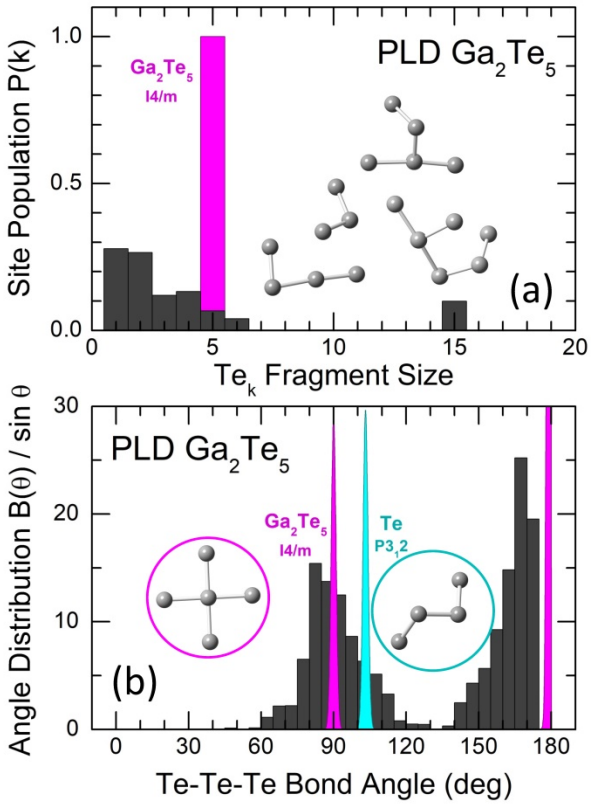

Figure 11. (**a**) Size and (**b**) Te-Te-Te bond angle distribution in Te_k oligomeric fragments, $k \leq 15$. The only population of 5-membered Te_5 square-planar fragments (crosses) in tetragonal Ga_2Te_5 is also shown in (**a**), as well as the characteristic $B_{TeTeTe}(\theta)/\sin\theta$ distributions in trigonal tellurium [57] and tetragonal Ga_2Te_5 [26]. Typical Te_k fragments in glassy and crystalline pentatellurides are shown in the insets, as well as a part of the helical tellurium chain in c-Te, $P3_12$ [57].

The intermediate-range order in glassy and amorphous materials is often described by ring statistics, that is, by the population of Ga_pTe_q rings in the case of gallium tellurides. The ring population $R_c(p + q)$ [54] in glassy Ga_2Te_5 (this work) and Ga_2Te_3 [16] PLD

films in comparison with crystalline references (tetragonal Ga_2Te_5 [26], cubic [17], and rhombohedral [89] Ga_2Te_3) is shown in Figure 12. The $R_c(p+q)$ population was found to be different for the two Ga_2Te_5 forms. The dominant eight-membered rings in tetragonal polymorphs are hardly populated in the PLD film. On the contrary, the most populated $p+q=5$ entities in g-Ga_2Te_5 are absent in c-Ga_2Te_5. The peritectic nature of tetragonal crystal seems to be related to this difference.

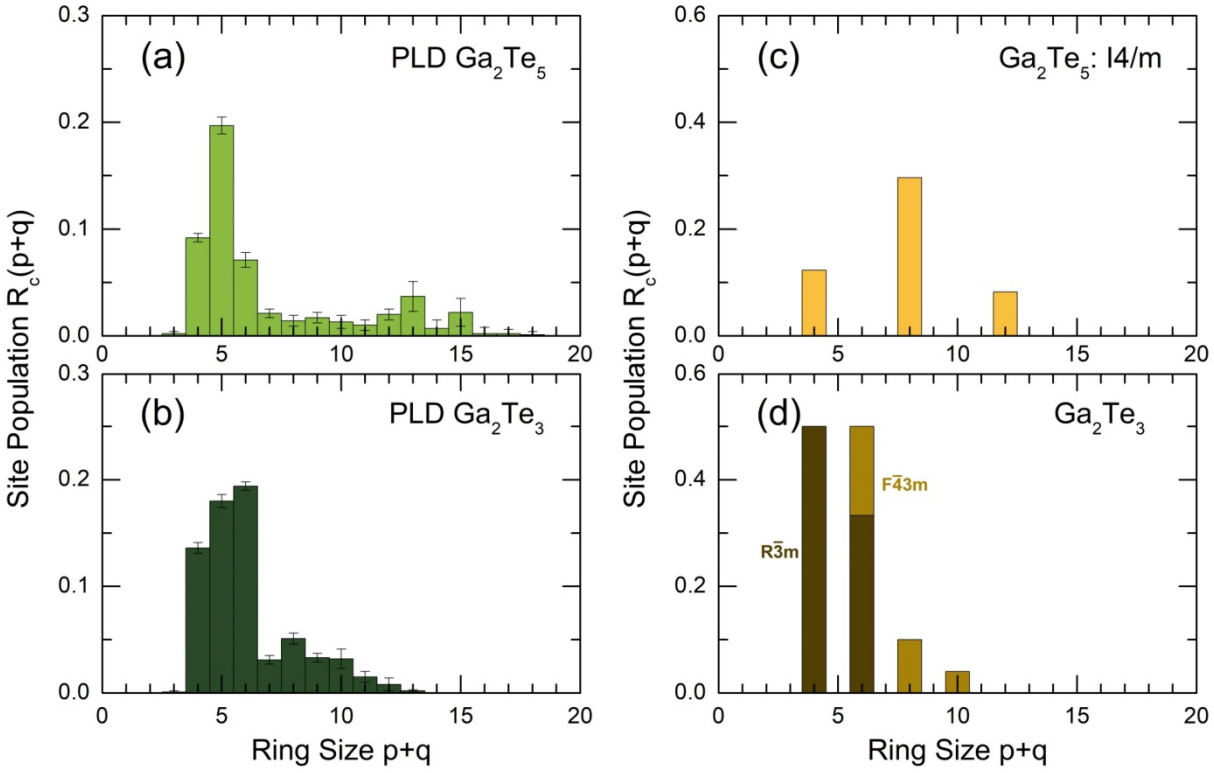

Figure 12. Ring population $R_c(p+q)$ [54] in glassy (**a**) Ga_2Te_5 (this work), (**b**) Ga_2Te_3 [16] PLD films, and crystalline references: (**c**) tetragonal Ga_2Te_5 [26], (**d**) cubic [17] and rhombohedral [89] Ga_2Te_3.

Gallium sesquitelluride Ga_2Te_3 is a congruently melting compound, Figure 1d. As it was reported earlier [16], the ring statistics in g-Ga_2Te_3 represent a disordered mixture of $R_c(p+q)$ for the ambient and high-pressure polymorphs, Figure 12b,d, related to nanotectonic contraction in a viscous supercooled melt.

Microscopic voids and cavities in amorphous Ga-Te alloys, obtained using the Dirichlet–Voronoi tessellation [56], are displayed in Figure 13b. The fraction of voids V_c, normalized to the volume of the FPMD simulation box, was found to be nearly invariant, $27 \leq V_c(x) \leq 29\%$, over the gallium content x between 0.20 (bulk g-$GaTe_4$) and 0.40 (PLD g-Ga_2Te_3). This is coherent with a small change in the number density, ≈2% over the same composition range. Typical cavity radius varies between 0.2 and 4 Å, slightly increasing with x, Figure 13a.

The total electronic density of states (eDOS) is shown in Figure 14 and appears to be typical for glassy and crystalline chalcogenides [15,16,59,90–92]. The valence band (VB) consists of three sub-bands between the Fermi level E_F and −16 eV. The upper part, roughly centered at −3 eV, mostly consists of Te 5p and Ga 4p states and also includes non-negligible d-electron contributions, as it revealed by the eDOS projections (pDOS) on Ga and Te atomic pseudo-wave functions. The middle-energy sub-band, centered at −8 eV, essentially contains Te 5p and Ga 4s electron states, while the lower part, peaked at −13 eV, has an s-character, populated by Te 5s electrons together with Ga s-, p- and d-electron contributions. The derived eDOS and pDOS are similar to those in g-Ga_2Te_3 PLD film [16] and suggest sp^3 gallium hybridization also has a d-electron contribution.

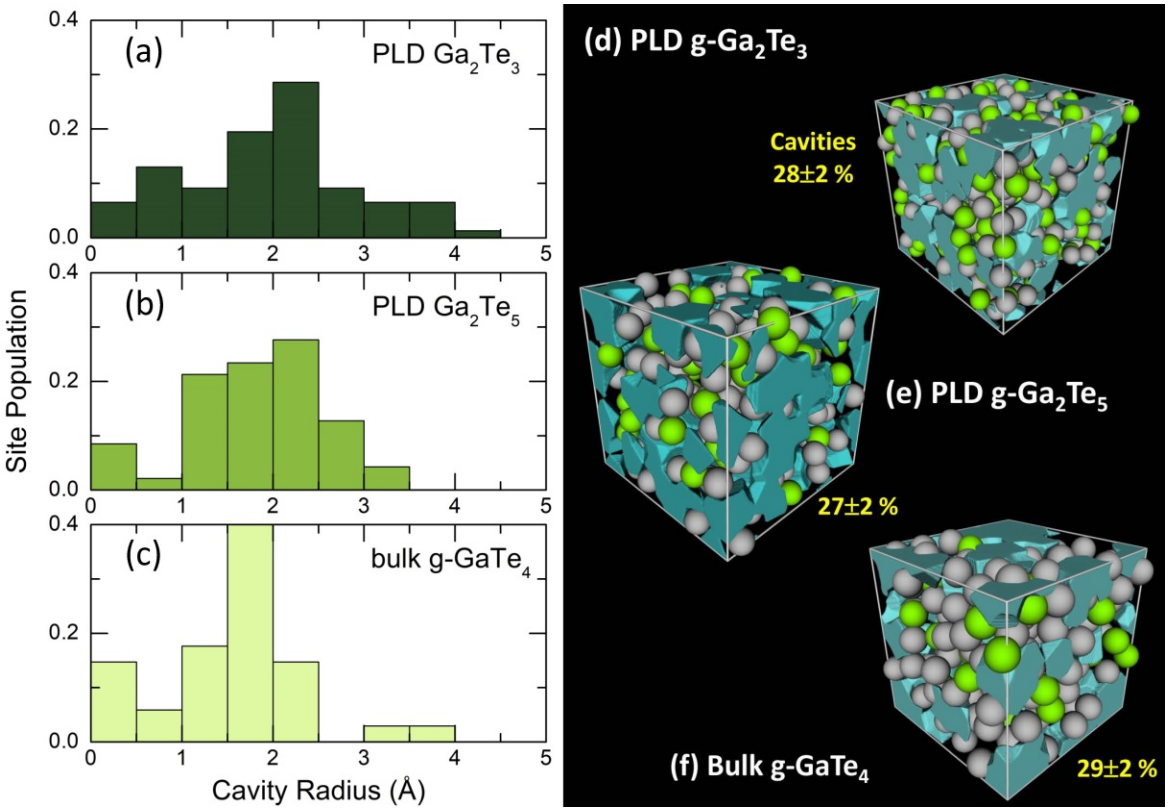

Figure 13. Microscopic voids in glassy Ga-Te alloys; typical distributions of characteristic cavity radii in (**a**) Ga_2Te_3, (**b**) Ga_2Te_5, and (**c**) $GaTe_4$; snapshots of simulation boxes with microscopic voids for (**d**) Ga_2Te_3 [16], (**e**) Ga_2Te_5 (this work), and (**f**) $GaTe_4$ [15], calculated using the Dirichlet–Voronoi approximation [56].

The inverse participation ratio IPR [93,94] allows for localized (large IPR $\rightarrow$ 1) and extended electron states (small IPR $\approx N^{-1}$, where N is the number of atoms in the simulation box) to be distinguished

$$\mathrm{IPR} = \frac{\int dr|\psi(r)|^4}{\left(\int dr|\psi(r)|^2\right)^2}, \tag{14}$$

where $\psi(r)$ is a single-particle Kohn–Sham eigenfunction. The calculated IPRs, derived using the projections of $\psi(r)$ onto an atomic basis set and the atomic orbital coefficients, are shown in Figure 14a, plotted together with the eDOS. As it was reported earlier [16,46], a higher electron localization appears at the band tails (the top of the valence and the bottom of the conduction bands), consistent with the theories of disordered semiconductors [59]. The remaining electron states in the vicinity of the bandgap are delocalized (extended). Deeper states of the lower-energy sub-bands, participating in the covalent bonding, are localized even more strongly.

The derived GGA/PBE0 bandgap, E_g^{PBE0} = 0.80 eV, appears to be smaller than the experimental optical bandgap, E_g = 0.98 eV, Figure 3b, but nearly identical to the interpolated electrical counterpart, $2E_a$ = 0.82 eV, Figure 2a. The main contribution of the Te 5p electron states to the upper part of the valence band and at the bottom of the conduction band is also consistent with a dominant role played by Te on the electronic conductivity of Ga-Te alloys, Figure 2b.

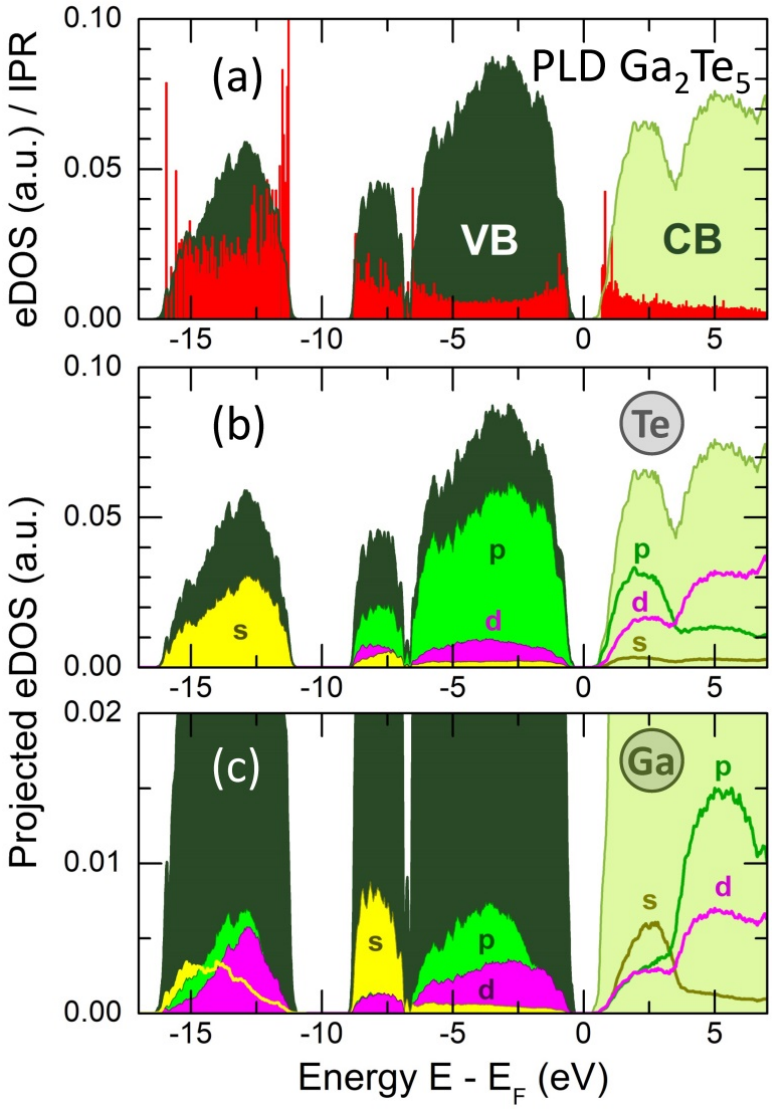

Figure 14. (**a**) Electronic density of states (eDOS) and inverse participation ratio (IPR, red spikes) in g-Ga_2Te_5 PLD film at 300 K, and projected DOS on (**b**) tellurium and (**c**) gallium atomic pseudo-wave functions. The s (yellow), p (green) and d (magenta) contributions are shown. VB = valence band; CB = conduction band.

7. Conclusions

Pulsed laser deposition allows for homogeneous and uniform Ga_2Te_5 films to be obtained, showing a distinct glass transition at 491 K and accompanied by strong crystallization peaked at 545 K. Thermal annealing of the PLD film with a DSC heating rate and carried out below the stability limits of tetragonal Ga_2Te_5 yields a high-quality and long-living (for at least 15 months) tetragonal polymorph that is thermodynamically metastable under ambient conditions. Amorphous and crystalline Ga_2Te_5 forms show reasonably high electric contrast (two orders of magnitude at room temperature) and distinctly different optical band gaps, E_g = 0.98 eV for g-Ga_2Te_5 and indirect optical bandgap E_g^i = 0.40 eV for c-Ga_2Te_5. Consequently, gallium pentatelluride can be used for memory applications as well as for photovoltaics, quantum-dots-based DNA sensors, and for the preparation of atomically thin layers via the controlled crystallization of amorphous thin films.

The local coordination of tetrahedral gallium is common for these two forms; however, the intermediate-range order and tellurium subnetwork are drastically different. Square-planar Te_5 units (crosses) connecting edge-sharing Ge-Te chains in tetragonal Ga_2Te_5, which are formed by ES-$GaTe_4$ tetrahedra, do not survive in the glassy polymorph, leaving Te_k

remnants, $3 \leq k \leq 6$, originating from the Te_5 entities and oligomeric tellurium chains similar to those in trigonal Te. Quasi-1D edge-sharing Ga-Te chains lose their exclusive structural signature, characteristic of tetragonal polymorph, transforming into 2D and 3D structural patches of edge- and corner-sharing $GaTe_4$ tetrahedra. The simulated electronic density of states is consistent with the experimental optical and conductivity results and reveals a predominant role of the Te 5p electron states for electronic properties of gallium pentatelluride.

Supplementary Materials: The following supporting information can be downloaded at: https://www.mdpi.com/article/10.3390/nano13142137/s1, Figure S1. X-ray diffraction patterns of rapidly cooled Ga_2Te_5 melt and Ga_2Te_5 PLD film; Figure S2. Scattering corrections for crystallized Ga_2Te_5 PLD film; Figure S3. FSDP parameters for glassy Ga_xTe_{1-x} alloys; Figure S4. Bond angle distribution $B_{\mathrm{TeGaTe}}(\theta)$ in simulated g-Ga_2Te_5.

Author Contributions: Conceptualization, E.B. and A.T.; HE-XRD, C.J.B.; synthesis, A.T., M.B., and M.K. (Mohammad Kassem); PLD, S.B.; FPMD, RMC, and statistics, M.K. (Maxim Khomenko), A.S., and D.F.; XRD, DSC, and conductivity, A.T., M.B., and M.K. (Mohammad Kassem); optics, A.T.; paper writing, E.B. with the help of all authors. All authors have read and agreed to the published version of the manuscript.

Funding: This work was supported by the Région Hauts de France and the Ministère de l'Enseignement Supérieur et de la Recherche (CPER ECRIN), as well as by the European Fund for Regional Economic Development. Work at the Advanced Photon Source, Argonne National Laboratory, was supported in part by the Office of Basic Energy Sciences, US Department of Energy, under Contract No. DE-AC02-06CH11357. M.K. (Maxim Khomenko) works at ILIT RAS, and TSU was supported by the Ministry of Science and Higher Education under agreement 075-15-2021-917; state assignment FSRC 'Crystallography and Photonics' Russian Academy of Sciences; and by the Tomsk State University Development Program (Priority-2030). SB's work was supported by the Estonian Research Council under grant number PRG1023. Partly, the measurements were carried out in the resource centers of St. Petersburg State University: "Centre for X-ray Diffraction Studies" and "Centre for Thermogravimetric and Calorimetric Research". This work was granted access to the HPC resources of IDRIS (France) under the allocation 2022-A0130910639 made by Grand Equipement National de Calcul Intensif (GENCI) and access to the use of the CALCULCO computing platform, supported by Service COmmun du Système d'Information de l'Université du Littoral Côte d'Opale (SCoSI/ULCO). The FPMD simulations were also carried out using the HPC computing resources at Lomonosov Moscow State University and at the ILIT RAS in Shatura (Moscow Region).

Data Availability Statement: The data presented in this study are available on request from the corresponding author.

Conflicts of Interest: The authors declare no conflict of interest.

References

1. Zhang, W.; Mazzarello, R.; Wuttig, M.; Ma, E. Designing crystallization in phase-change materials for universal memory and neuro-inspired computing. *Nat. Rev. Mater.* **2019**, *4*, 150–168. [CrossRef]
2. Xu, M.; Mai, X.; Lin, J.; Zhang, W.; Li, Y.; He, Y.; Tong, H.; Hou, X.; Zhou, P.; Miao, X. Recent advances on neuromorphic devices based on chalcogenide phase-change materials. *Adv. Funct. Mater.* **2020**, *30*, 2003419. [CrossRef]
3. Feldmann, J.; Youngblood, N.; Karpov, M.; Gehring, H.; Li, X.; Stappers, M.; Le Gallo, M.; Fu, X.; Lukashchuk, A.; Raja, A.S.; et al. Parallel convolutional processing using an integrated photonic tensor core. *Nature* **2021**, *589*, 52–61. [CrossRef]
4. Wang, Q.; Rogers, E.T.F.; Gholipour, B.; Wang, C.-M.; Yuan, G.; Teng, J.; Zheludev, N.I. Optically reconfigurable metasurfaces and photonic devices based on phase change materials. *Nat. Photon.* **2016**, *10*, 60–66. [CrossRef]
5. Shalaginov, M.Y.; An, S.; Zhang, Y.; Yang, F.; Su, P.; Liberman, V.; Chou, J.B.; Roberts, C.M.; Kang, M.; Rios, C.; et al. Reconfigurable all-dielectric metalens with diffraction-limited performance. *Nat. Commun.* **2021**, *12*, 1225. [CrossRef]
6. Konnikova, M.R.; Khomenko, M.D.; Tverjanovich, A.S.; Bereznev, S.; Mankova, A.A.; Parashchuk, O.D.; Vasilevsky, I.S.; Ozheredov, I.A.; Shkurinov, A.P.; Bychkov, E.A. $GeTe_2$ phase change material for terahertz devices with reconfigurable functionalities using optical activation. *ACS Appl. Mater. Interfaces* **2023**, *15*, 9638–9648. [CrossRef]
7. Dong, W.; Liu, H.; Behera, J.K.; Lu, L.; Ng, R.J.H.; Sreekanth, K.V.; Zhou, X.; Yang, J.K.W.; Simpson, R.E. Wide bandgap phase change material tuned visible photonics. *Adv. Funct. Mater.* **2019**, *29*, 1806181. [CrossRef]

8. Liu, H.; Dong, W.; Wang, H.; Lu, L.; Ruan, Q.; Tan, Y.S.; Simpson, R.E.; Yang, J.K.W. Rewritable color nanoprints in antimony trisulfide films. *Sci. Adv.* **2020**, *6*, eabb7171. [CrossRef]
9. Delaney, M.; Zeimpekis, I.; Lawson, D.; Hewak, D.W.; Muskens, O.L. A new family of ultralow loss reversible phase-change materials for photonic integrated circuits: Sb_2S_3 and Sb_2Se_3. *Adv. Funct. Mater.* **2020**, *30*, 2002447. [CrossRef]
10. Ilie, S.T.; Faneca, J.; Zeimpekis, I.; Domínguez Bucio, T.; Grabska, K.; Hewak, D.W.; Chong, H.M.H.; Gardes, F.Y. Thermo-optic tuning of silicon nitride microring resonators with low loss non-volatile Sb_2S_3 phase change material. *Sci. Rep.* **2022**, *12*, 17815. [CrossRef]
11. Zhu, H.; Yin, J.; Xia, Y.; Liu, Z. Ga_2Te_3 phase change material for low-power phase change memory application. *Appl. Phys. Lett.* **2010**, *97*, 083504. [CrossRef]
12. Lee, D.; Kim, T.; Sohn, H. Highly reliable threshold switching behavior of amorphous Ga_2Te_3 films deposited by RF sputtering. *Appl. Phys. Express* **2019**, *12*, 085504. [CrossRef]
13. Lee, D.; Kim, T.; Kim, J.; Sohn, H. Effect of nitrogen doping on threshold voltage in amorphous Ga_2Te_3 for application of selector devices. *Phys. Status Solidi A* **2020**, *217*, 2000478. [CrossRef]
14. Kolobov, A.V.; Fons, P.; Krbal, M.; Mitrofanov, K.; Tominaga, J.; Uruga, T. Local structure of the crystalline and amorphous states of Ga_2Te_3 phase-change alloy without resonant bonding: A combined X-ray absorption and ab initio study. *Phys. Rev. B* **2017**, *95*, 054114. [CrossRef]
15. Bokova, M.; Tverjanovich, A.; Benmore, C.J.; Fontanari, D.; Sokolov, A.; Khomenko, M.; Kassem, M.; Ozheredov, I.; Bychkov, E. Unraveling the atomic structure of bulk binary Ga-Te glasses with surprising nanotectonic features for phase-change memory applications. *ACS Appl. Mater. Interfaces* **2021**, *13*, 37363–37379. [CrossRef]
16. Tverjanovich, A.; Khomenko, M.; Benmore, C.J.; Bereznev, S.; Sokolov, A.; Fontanari, D.; Kiselev, A.; Lotin, A.; Bychkov, E. Atypical phase-change alloy Ga_2Te_3: Atomic structure, incipient nanotectonic nuclei, and multilevel writing. *J. Mater. Chem. C* **2021**, *9*, 17019–17032. [CrossRef]
17. Guymont, M.; Tomas, A.; Guittard, M. The structure of Ga_2Te_3. An X-ray and high-resolution electron microscopy study. *Philos. Mag. A* **1992**, *66*, 133–139. [CrossRef]
18. Glazov, V.M.; Chizhevskaya, S.N.; Glagoleva, N.N. *Liquid Semiconductors*; Plenum: New York, NY, USA, 1969; pp. 142–150.
19. Chizhevskaya, S.N.; Glazov, V.M. A study of chemical interactions between gallium and tellurium in molten state. *Zh. Neorg. Khim.* **1962**, *7*, 1933–1937.
20. Ito, K.; Moynihan, C.T.; Angell, C.A. Thermodynamic determination of fragility in liquids and a fragile-to-strong liquid transition in water. *Nature* **1999**, *398*, 492–495. [CrossRef]
21. Wei, S.; Lucas, P.; Angell, C.A. Phase change alloy viscosities down to T_g using Adam-Gibbs-equation fittings to excess entropy data: A fragile-to-strong transition. *J. Appl. Phys.* **2015**, *118*, 034903. [CrossRef]
22. Orava, J.; Hewak, D.W.; Greer, A.L. Fragile-to-strong crossover in supercooled liquid Ag-In-Sb-Te studied by ultrafast calorimetry. *Adv. Funct. Mater.* **2015**, *25*, 4851–4858. [CrossRef]
23. Zhu, W.; Gulbiten, O.; Aitken, B.; Sen, S. Viscosity, enthalpy relaxation and liquid-liquid transition of the eutectic liquid $Ge_{15}Te_{85}$. *J. Non-Cryst. Solids* **2021**, *554*, 120601. [CrossRef]
24. Kassem, M.; Benmore, C.J.; Usuki, T.; Ohara, K.; Tverjanovich, A.; Bokova, M.; Brazhkin, V.V.; Bychkov, E. Transient mesoscopic immiscibility, viscosity anomaly and high internal pressure at the semiconductor-metal transition in liquid Ga_2Te_3. *J. Phys. Chem. Lett.* **2022**, *13*, 10843–10850. [CrossRef]
25. Taylor, G.I. The viscosity of a fluid containing small drops of another fluid. *Proc. R. Soc. Lond. Ser. A* **1932**, *138*, 41–48.
26. Julien-Pouzol, M.; Jaulmes, S.; Alapini, F. Tellurure de gallium. *Acta Crystallogr. B* **1977**, *33*, 2270–2272. [CrossRef]
27. Deiseroth, H.J.; Amann, P. Die Pentatelluride M_2Te_5 (M = Al, Ga, In): Polymorphie, Struktur-beziehungen und Homogenitäts-bereiche. *Z. Anorg. Allg. Chem.* **1996**, *622*, 985–993. [CrossRef]
28. Kolobov, A.V.; Tominaga, J. *Chalcogenides: Metastability and Phase Change Phenomena*; Springer: Berlin, Germany, 2012; pp. 30, 181–208.
29. Hilmi, I.; Lotnyk, A.; Gerlach, J.W.; Schumacher, P.; Rauschenbach, B. Research update: Van-der-Waals epitaxy of layered chalcogenide Sb_2Te_3 thin films grown by pulsed laser deposition. *APL Mater.* **2017**, *5*, 050701. [CrossRef]
30. Alapini, F.; Flahaut, J.; Guittard, M.; Jaulmes, S.; Julien-Pouzol, M. Système gallium–tellure. Diagramme de phases, étude structurale de GaTe, Ga_2Te_5 et de Ga_6SnTe_{10}. *J. Solid State Chem.* **1979**, *28*, 309–319. [CrossRef]
31. Blachnik, R.; Irle, E. Das System Gallium–Tellur. *J. Less-Common Met.* **1985**, *113*, L1–L3. [CrossRef]
32. Oh, C.-S.; Lee, D.N. Thermodynamic assessment of the Ga-Te system. *Calphad* **1992**, *16*, 317–330.
33. Fu, H.; Ying, P.; Cui, J.; Zhang, X.; Yan, Y. Thermoelectric properties of p-type Ga_2Te_5 based compounds. *Rare Metal Mater. Eng.* **2012**, *41*, 767–771. [CrossRef]
34. Fuku, X.; Baker, P.; Iwuoha, E. Influence of quantum dot surface on electrochemical DNA sensing mechanism. *ChemElectroChem* **2020**, *7*, 770–781. [CrossRef]
35. Siddique, S.; Gowda, C.C.; Tromer, R.; Demiss, S.; Singh Gautam, A.R.; Femi, O.E.; Kumbhakar, P.; Galvao, D.S.; Chandra, A.; Tiwary, C.S. Scalable synthesis of atomically thin gallium telluride nanosheets for supercapacitor applications. *ACS Appl. Nano Mater.* **2021**, *4*, 4829–4838. [CrossRef]
36. Hoang Huy, V.P.; Kim, I.T.; Hur, J. Gallium-telluride-based composite as promising lithium storage material. *Nanomaterials* **2022**, *12*, 3362. [CrossRef]

37. Guan, J.; Sun, C.; Zhang, C.; Guan, Q.; Kan, E. First-principles calculations of monolayered Al_2Te_5: A promising 2D donor semiconductor with ultrahigh visible light harvesting. *Nanoscale* **2023**, *15*, 2578–2585. [CrossRef] [PubMed]
38. Tverjanovich, A.; Khomenko, M.; Bereznev, S.; Fontanari, D.; Sokolov, A.; Usuki, T.; Ohara, K.; Le Coq, D.; Masselin, P.; Bychkov, E. Glassy GaS: Transparent and unusually rigid thin films for visible to mid-IR memory applications. *Phys. Chem. Chem. Phys.* **2020**, *22*, 25560–25573. [CrossRef] [PubMed]
39. Hammersley, A.P.; Svensson, S.O.; Hanfland, M.; Fitch, A.N.; Häusermann, D. Two-dimensional detector software: From real detector to idealised image or two-theta scan. *High Press. Res.* **1996**, *14*, 235–248. [CrossRef]
40. Skinner, L.B.; Benmore, C.J.; Parise, J.B. Area detector corrections for high quality synchrotron X-ray structure factor measurements. *Nucl. Instrum. Methods Phys. Res.* **2012**, *662*, 61–70. [CrossRef]
41. Kühne, T.D.; Iannuzzi, M.; Del Ben, M.; Rybkin, V.V.; Seewald, P.; Stein, F.; Laino, T.; Khaliullin, R.Z.; Schütt, O.; Schiffmann, F.; et al. CP2K: An electronic structure and molecular dynamics software package—Quickstep: Efficient and accurate electronic structure calculations. *J. Chem. Phys.* **2020**, *152*, 194103. [CrossRef]
42. Perdew, J.P.; Ernzerhof, M.; Burke, K. Rationale for mixing exact exchange with density functional approximations. *J. Chem. Phys.* **1996**, *105*, 9982–9985. [CrossRef]
43. Adamo, C.; Barone, V. Toward reliable density functional methods without adjustable parameters: The PBE0 model. *J. Chem. Phys.* **1999**, *110*, 6158–6170. [CrossRef]
44. Tverjanovich, A.; Khomenko, M.; Benmore, C.J.; Bokova, M.; Sokolov, A.; Fontanari, D.; Kassem, M.; Usuki, T.; Bychkov, E. Bulk glassy $GeTe_2$: A missing member of the netrahedral GeX_2 family and a precursor for the next generation of phase-change materials. *Chem. Mater.* **2021**, *33*, 1031–1045. [CrossRef]
45. Kassem, M.; Bounazef, T.; Sokolov, A.; Bokova, M.; Fontanari, D.; Hannon, A.C.; Alekseev, I.; Bychkov, E. Deciphering fast ion transport in glasses: A case study of sodium and silver vitreous sulfides. *Inorg. Chem.* **2022**, *61*, 12870–12885. [CrossRef]
46. Kassem, M.; Benmore, C.J.; Tverjanovich, A.; Usuki, T.; Khomenko, M.; Fontanari, D.; Sokolov, A.; Ohara, K.; Bokova, M.; Kohara, S.; et al. Glassy and liquid Sb_2S_3: Insight into the structure and dynamics of a promising functional material. *J. Mater. Chem. C* **2023**, *11*, 4654–4673. [CrossRef]
47. Grimme, S.; Ehrlich, S.; Goerigk, L. Effect of the damping function in dispersion corrected density functional theory. *J. Comput. Chem.* **2011**, *32*, 1456–1465. [CrossRef]
48. Micoulaut, M. Communication: Van der Waals corrections for an improved structural description of telluride based materials. *J. Chem. Phys.* **2013**, *138*, 061103. [CrossRef] [PubMed]
49. Bouzid, A.; Massobrio, C.; Boero, M.; Ori, G.; Sykina, K.; Furet, E. Role of the van der Waals interactions and impact of the exchange-correlation functional in determining the structure of glassy $GeTe_4$. *Phys. Rev. B* **2015**, *92*, 134208. [CrossRef]
50. Gereben, O.; Pusztai, L. RMC_POT, a computer code for reverse Monte Carlo modeling the structure of disordered systems containing molecules of arbitrary complexity. *J. Comput. Chem.* **2012**, *33*, 2285–2291. [CrossRef] [PubMed]
51. Hartwigsen, C.; Goedecker, S.; Hutter, J. Relativistic separable dual-space Gaussian pseudo-potentials from H to Rn. *Phys. Rev. B* **1998**, *58*, 3641. [CrossRef]
52. Nosé, S. A Molecular dynamics method for simulations in the canonical ensemble. *Mol. Phys.* **1984**, *52*, 255–268. [CrossRef]
53. Hoover, W.G. Canonical dynamics: Equilibrium phase-space distributions. *Phys. Rev. A* **1985**, *31*, 1695. [CrossRef] [PubMed]
54. Le Roux, S.; Jund, P. Ring statistics analysis of topological networks: New approach and application to amorphous GeS_2 and SiO_2 systems. *Comput. Mater. Sci.* **2010**, *49*, 70–83. [CrossRef]
55. Kohara, S.; Ohno, H.; Takata, M.; Usuki, T.; Morita, H.; Suzuya, K.; Akola, J.; Pusztai, L. Lead silicate glasses: Binary network-former glasses with large amounts of free volume. *Phys. Rev. B* **2010**, *82*, 134209. [CrossRef]
56. Heimbach, I.; Rhiem, F.; Beule, F.; Knodt, D.; Heinen, J.; Jones, R.O. pyMolDyn: Identification, structure, and properties of cavities/vacancies in condensed matter and molecules. *J. Comput. Chem.* **2017**, *38*, 389–394. [CrossRef]
57. Cherin, P.; Unger, P. Two-dimensional refinement of the crystal structure of tellurium. *Acta Crystallogr.* **1967**, *23*, 670–671. [CrossRef]
58. Nassary, M.M.; Gerges, M.K.; Shaban, H.T.; Salwa, A.S. Some physical properties of Ga_2Te_5 single crystals. *Phys. B* **2003**, *337*, 130–137. [CrossRef]
59. Mott, N.F.; Davis, E.A. *Electronic Processes in Non-Crystalline Materials*, 2nd ed.; Clarendon Press: Oxford, UK, 1979; pp. 5–64, 491–497.
60. Ray, A.K.; Swan, R.; Hogarth, C.A. Conduction mechanisms in amorphous tellurium films. *J. Non-Cryst. Solids* **1994**, *168*, 150–156. [CrossRef]
61. Bekheet, A.E. Electrical and optical properties of amorphous Ga_2Te_3 films. *Eur. Phys. J. Appl. Phys.* **2001**, *16*, 187–193. [CrossRef]
62. Swanepoel, R. Determination of the thickness and optical constants of amorphous silicon. *J. Phys. E Sci. Instrum.* **1983**, *16*, 1214–1222. [CrossRef]
63. Jenkins, F.A.; White, H.E. *Fundamentals of Optics*, 4th ed.; McGraw-Hill: New York, NY, USA, 2001; pp. 479–485.
64. Tauc, J. Optical properties of amorphous semiconductors. In *Amorphous and Liquid Semiconductors*; Tauc, J., Ed.; Plenum: London, UK, 1974; pp. 159–220.

65. Heller, W.; Bhatnagar, H.L.; Nakagaki, M. Theoretical investigations on the light scattering of spheres. XIII. The "wavelength exponent" of differential turbidity spectra. *J. Chem. Phys.* **1962**, *36*, 1163–1170. [CrossRef]
66. Melik, D.H.; Fogler, H.S. Turbidimetric determination of particle size distributions of colloidal systems. *J. Colloid Interface Sci.* **1983**, *92*, 161–180. [CrossRef]
67. Green, M.A.; Keevers, M.J. Optical properties of intrinsic silicon at 300 K. *Prog. Photovolt. Res. Appl.* **1995**, *3*, 189–192. [CrossRef]
68. Zacharias, M.; Feliciano Giustino, F. One-shot calculation of temperature-dependent optical spectra and phonon-induced band-gap renormalization. *Phys. Rev. B* **2016**, *94*, 075125. [CrossRef]
69. Koughia, K.; Singh, J.; Kasap, S.O.; Ruda, H.E. Fundamental optical properties of materials II. In *Optical Properties of Condensed Matter and Applications*; Singh, J., Ed.; Wiley: Chichester, UK, 2006; pp. 27–46.
70. Noffsinger, J.; Kioupakis, E.; Van de Walle, C.G.; Louie, S.G.; Cohen, M.L. Phonon-assisted optical absorption in silicon from first principles. *Phys. Rev. Lett.* **2012**, *108*, 167402. [CrossRef] [PubMed]
71. Zacharias, M.; Patrick, C.E.; Giustino, F. Stochastic approach to phonon-assisted optical absorption. *Phys. Rev. Lett.* **2015**, *115*, 177401. [CrossRef] [PubMed]
72. Kangsabanik, J.; Svendsen, M.K.; Taghizadeh, A.; Crovetto, A.; Thygesen, K.S. Indirect band gap semiconductors for thin-film photovoltaics: High-throughput calculation of phonon-assisted absorption. *J. Am. Chem. Soc.* **2022**, *144*, 19872–19883. [CrossRef]
73. Bullett, D.W. Square-planar coordinated tellurides—The electronic structures of Re_2Te_5, Ga_2Te_5 and K_2SnTe_5. *Solid State Commun.* **1984**, *51*, 51–53. [CrossRef]
74. Bychkov, E.; Benmore, C.J.; Price, D.L. Compositional changes of the first sharp diffraction peak in binary selenide glasses. *Phys. Rev. B* **2005**, *72*, 172107. [CrossRef]
75. Bytchkov, A.; Cuello, G.J.; Kohara, S.; Benmore, C.J.; Price, D.L.; Bychkov, E. Unraveling the atomic structure of Ge-rich sulfide glasses. *Phys. Chem. Chem. Phys.* **2013**, *15*, 8487–8494. [CrossRef]
76. Hannon, A.C. XTAL: A Program for Calculating Interatomic Distances and Coordination Numbers for Model Structures; Rutherford-Appleton Laboratory Report RAL-93−063, 1993. Available online: http://wwwisis2.isis.rl.ac.uk/disordered/ACH/Software/xtal.htm (accessed on 22 May 2023).
77. Voleská, I.; Akola, J.; Jóvári, P.; Gutwirth, J.; Wágner, T.; Vasileiadis, T.; Yannopoulos, S.N.; Jones, R.O. Structure, electronic, and vibrational properties of glassy $Ga_{11}Ge_{11}Te_{78}$: Experimentally constrained density functional study. *Phys. Rev. B* **2012**, *86*, 094108. [CrossRef]
78. Pethes, I.; Piarristeguy, A.; Pradel, A.; Michalik, S.; Nemausat, R.; Darpentigny, J.; Jóvári, P. Short range order and topology of $Ge_xGa_xTe_{100-2x}$ glasses. *J. Alloys Compd.* **2020**, *834*, 155097. [CrossRef]
79. Ichikawa, T. Electron diffraction study of the local atomic arrangement in amorphous tellurium films. *Phys. Stat. Solidi B* **1973**, *56*, 707–715. [CrossRef]
80. Brazhkin, V.V.; Bychkov, E.; Tsiok, O.B. As_2Te_3 glass under high hydrostatic pressure: Polyamorphism, relaxation, and metallization. *Phys. Rev. B* **2017**, *95*, 054205. [CrossRef]
81. Chau, P.-L.; Hardwick, A.J. A new order parameter for tetrahedral configurations. *Mol. Phys.* **1998**, *93*, 511–518. [CrossRef]
82. Errington, J.R.; Debenedetti, P.G. Relationship between structural order and the anomalies of liquid water. *Nature* **2001**, *409*, 318–321. [CrossRef]
83. Caravati, S.; Bernasconi, M.; Kühne, T.D.; Krack, M.; Parrinello, M. Coexistence of tetrahedral- and octahedrallike sites in amorphous phase change materials. *Appl. Phys. Lett.* **2007**, *91*, 171906. [CrossRef]
84. Akola, J.; Jones, R.O. Binary alloys of Ge and Te: Order, voids, and the eutectic composition. *Phys. Rev. Lett.* **2008**, *100*, 205502. [CrossRef]
85. Caravati, S.; Bernasconi, M. Influence of the exchange and correlation functional on the structure of amorphous $Ge_2Sb_2Te_5$. *Phys. Stat. Solidi B* **2015**, *252*, 260–266. [CrossRef]
86. Raty, J.Y.; Zhang, W.; Luckas, J.; Chen, C.; Mazzarello, R.; Bichara, C.; Wuttig, M. Aging mechanisms in amorphous phase-change materials. *Nat. Commun.* **2015**, *6*, 7467. [CrossRef]
87. Micoulaut, M.; Piarristeguy, A.; Flores-Ruiz, H.; Pradel, A. Towards accurate models for amorphous GeTe: Crucial effect of dispersive van der Waals corrections on the structural properties involved in the phase-change mechanism. *Phys. Rev. B* **2017**, *96*, 184204. [CrossRef]
88. Jones, C.Y.; Bryan, J.C.; Kirschbaum, K.; Edwards, J.G. Refinement of the crystal structure of digallium trisulfide, Ga_2S_3. *Z. Kristallogr. NCS* **2001**, *216*, 327–328. [CrossRef]
89. Serebryanaya, N.R. The crystal structure of pressure-induced phases of In_2Te_3 and Ga_2Te_3. *Powder Diffr.* **1992**, *7*, 99–102. [CrossRef]
90. Blaineau, S.; Jund, P. Electronic structure of amorphous germanium disulfide via density-functional molecular dynamics simulations. *Phys. Rev. B* **2004**, *70*, 184210. [CrossRef]
91. Akola, J.; Jones, R.O. Structural phase transitions on the nanoscale: The crucial pattern in the phase-change materials $Ge_2Sb_2Te_5$ and GeTe. *Phys. Rev. B* **2007**, *76*, 235201. [CrossRef]
92. Dragoni, D.; Gabardi, S.; Bernasconi, M. First-principles study of the liquid and amorphous phases of In_2Te_3. *Phys. Rev. Mater.* **2017**, *1*, 035603. [CrossRef]

93. Kalikka, J.; Akola, J.; Jones, R.O.; Kohara, S.; Usuki, T. Amorphous $Ge_{15}Te_{85}$: Density functional, high-energy X-ray and neutron diffraction study. *J. Phys. Condens. Matter* **2012**, *24*, 015802. [CrossRef]
94. Caravati, S.; Bernasconi, M.; Parrinello, M. First-principles study of liquid and amorphous Sb_2Te_3. *Phys. Rev. B* **2010**, *81*, 014201. [CrossRef]